DYNAMIC PULSED BEAM STEERING USING VIRTUALLY IMAGED PHASED ARRAY

by

Jie Wang

A Thesis

Submitted to the Faculty of Purdue University

In Partial Fulfillment of the Requirements for the degree of

Master of Science in Electrical and Computer Engineering

School of Electrical and Computer Engineering

West Lafayette, Indiana

August 2023

THE PURDUE UNIVERSITY GRADUATE SCHOOL
STATEMENT OF COMMITTEE APPROVAL

Dr. Andrew M. Weiner, Chair

School of Electrical and Computer Engineering

Dr. Jason D. McKinney

School of Electrical and Computer Engineering

Dr. Minghao Qi

School of Electrical and Computer Engineering

Dr. Sunil A. Bhave

School of Electrical and Computer Engineering

Approved by:

Dr. Milind Kulkarni

ACKNOWLEDGMENTS

First and foremost, I would like to thank Prof. Andrew M. Weiner for not only providing me with the valuable opportunity to work on this exciting research project but also for his insightful guidance and timely feedback and suggestions. I would like to thank Suparna Seshadri for her invaluable mentorship and support throughout the experiments. Her guidance, patience, and constant encouragement helped me navigate through the challenges of this research. I would also like to extend my sincere appreciation to the other group members, Dr. Kaiyi Wu, Nathan O'Malley, Saleha Fatema, Vivek V. Wankhade, Lucas Cohen, Ryan Schneider, Alexandria Moore, Karthik V. Myilswamy, and Stephen Chapman. Their assistance and discussions have greatly enriched my graduate study experience. Furthermore, I would like to acknowledge the members of my thesis defense committee, Prof. Jason D. McKinney, Prof. Minghao Qi, and Prof. Sunil A. Bhave, for their valuable time, insightful comments and suggestions.

Lastly, I would like to thank my family and friends for their unwavering support, understanding, and encouragement throughout this challenging yet rewarding journey.

TABLE OF CONTENTS

LIST OF FIGURES

ABBREVIATIONS

LiDAR	Light Detection and Ranging
MEMS	Microelectromechanical System
OPA	Optical Phased Array
VIPA	Virtually Imaged Phased Array
CEO	Carrier-Envelope Offset
WDM	Wavelength-Division Multiplexing
FMCW	Frequency-Modulated Continuous-Wave
ASE	Amplified Stimulated Emission
OSA	Optical Spectrum Analyzer
FSR	Free Spectral Range
FWHM	Full Width at Half Maximum
EO Comb	Electro-Optic Comb
CW	Continuous Wave
RF	Radio Frequency
PM	Phase Modulator
IM	Intensity Modulator

ABSTRACT

Optical beam steering is of significant importance for various emerging applications such as light detection and ranging (LiDAR), free space optical communication, and holographic display. However, the development of schemes for dynamic spatio-temporal beam steering has been limited in the past. A previous study achieved dynamic and continuous angular beam steering of isolated ultrashort pulses from a mode-locked laser by using a passive metasurface emulating a diffraction grating followed by a lens. In this thesis, we experimentally demonstrate dynamic spatio-temporal steering of high repetition rate pulse trains using a spatial array of frequency combs with a uniform gradient in their carrier-envelope offsets. To accomplish this, we leverage the capabilities of a virtually imaged phased array (VIPA), which is a side-entrance Fabry-Perot etalon, and employ successive spatial Fourier transforms facilitated by a 4f optical lens system. Our experimental results successfully demonstrate the periodic scanning of ultrashort pulse trains generated from an electro-optic comb at a repetition rate of $\sim$ 10 GHz. The scanning occurs in discrete steps of $\sim$ 115 μm and $\sim$ 20 ps in the spatial and temporal domains, respectively.

1. INTRODUCTION

1.1 Dynamic Pulsed Beam Steering

Optical beam steering is of significant importance for various emerging applications such as light detection and ranging (LiDAR) [1], free space optical communication [2], and holographic display [3]. Conventional macromechanical scanners are bulky, slow, and lack mechanical durability, while more compact microelectromechanical systems (MEMS) still suffer from vulnerability to the environment with the moving parts, and liquid crystal based systems are limited by the long response times [4], [5]. There has been rapid development in nanophotonics based beam steering devices in recent years, including integrated optical phased arrays (OPAs) [6] and active phase gradient metasurfaces [7]. These advancements show promise in terms of both compact size and high-speed operation.

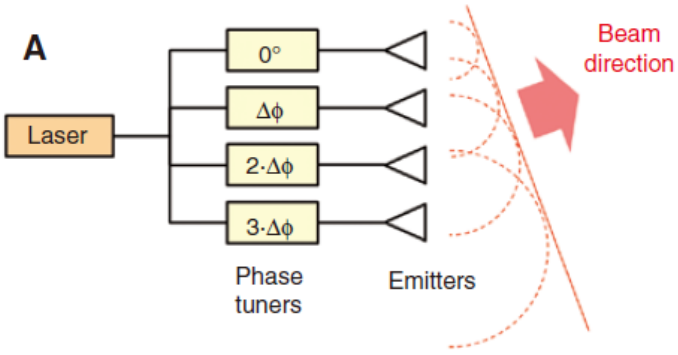

Figure 1.1. General schematic of an optical phased array. [8]

The general schematic of an OPA is illustrated in Figure. 1.1. The coherent laser source is divided into an array of optical emitters. A phase gradient is then applied across the array using phase tuners. In the far field, similar to the RF phased array, the uniformly delayed emitted beams coherently combine to form a flat wavefront with the propagation direction perpendicular to it. Consider a uniformly spaced array of identical emitters with a

radiation pattern described by $G(\vec{r})$, the far field expression is given by (with approximation $|\vec{r} - \vec{r_n}| = r + nd\sin\theta$) [9]

$$\begin{aligned} E(\vec{r},t) &= G(\vec{r})\mathrm{e}^{\mathrm{i}(kr-wt)}F(u) = G(\vec{r})\mathrm{e}^{\mathrm{i}(kr-wt)}\sum_{n=-N}^{N}\mathrm{e}^{\mathrm{i}nu} \\ &= G(\vec{r})\mathrm{e}^{\mathrm{i}(kr-wt)}\sum_{n=-N}^{N}\mathrm{e}^{\mathrm{i}n(kd\sin\theta-\Delta\alpha)} \end{aligned} \tag{1.1}$$

here $F(u) = \sum_{n=-N}^{N}\mathrm{e}^{\mathrm{i}nu}$ is the array factor, where $u = kd\sin\theta - \Delta\alpha$, d is the array spacing and $\Delta\alpha$ is the phase gradient. The summation of the array factor yields

$$|F(u)| = \left|\frac{\sin(Nu/2)}{\sin(u/2)}\right| \tag{1.2}$$

The maxima of the equation is $u = 2m\pi, m \in \mathbb{Z}$. Then for a phase gradient of $\Delta\theta$ the emitted beam direction θ is given by

$$\sin\theta = \frac{\Delta\alpha + 2m\pi}{kd} \qquad m \in \mathbb{Z} \tag{1.3}$$

Therefore, beam steering can be achieved by actively adjusting the applied phase gradient. A typical OPA system [10] is shown in Figure. 1.2. It is capable of 2D beam steering and is fabricated on silicon-on-insulator (SOI). The laser light was coupled into a waveguide through a lens fiber and then split into 16 parallel waveguides using a multimode interference (MMI) coupler tree. The phase was controlled thermo-optically by a titanium electrode on top of the structure, which has a uniform length gradient across the waveguide array. The light was subsequently coupled out through the grating couplers. By changing the current flowing through the titanium heating element, a uniform phase gradient is induced through silicon's relatively large thermo-optic coefficient. This leads to beam steering in the direction perpendicular to the waveguide array (steering angle ϕ). Tuning the wavelength allows for beam steering along the direction of the waveguides, with the steering angle θ determined by the grating equation. Another OPA system [11], shown in Figure. 1.3, utilizes electro-optic p-i-n phase modulators to achieve higher speed and lower power consumption.

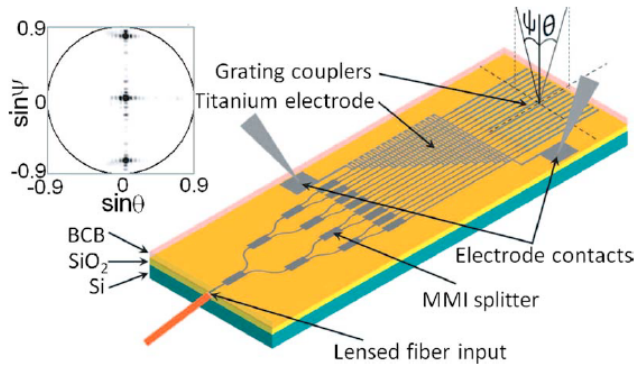

Figure 1.2. Schematic of a typical OPA system capable of 2D beam steering by thermo-optical phase control and wavelength tuning. [10]

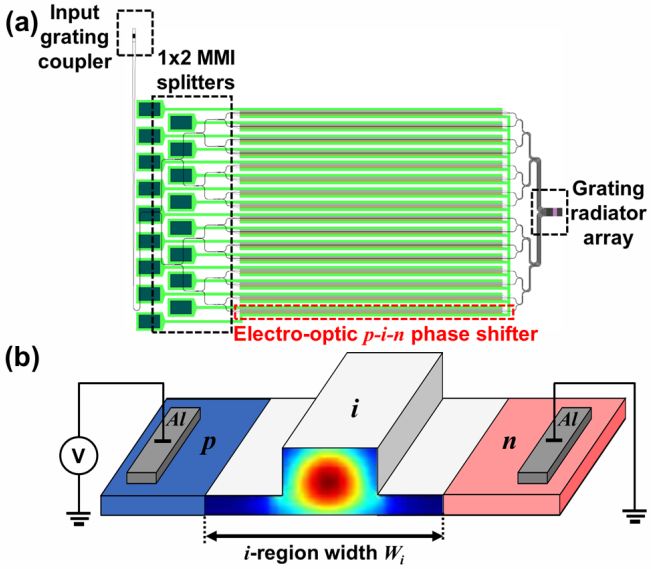

Figure 1.3. Schematic of an OPA system capable of 2D beam steering by electro-optic phase control and wavelength tuning. [11]

While most chip-scale architectures achieve quasi-static beam control by relying on external phase control or wavelength tuning, the development of schemes for dynamic spatio-temporal beam steering has been limited in the past. In a previous work [12], dynamic and continuous angular beam steering of isolated ultrashort pulses was achieved based on a virtual frequency-gradient metasurface, which was implemented using a mode-locked laser and a passive metasurface emulating a diffraction grating followed by a lens. As illustrated

in Figure. 1.4, the frequency gradient results in a linear time-dependent phase difference between the emitters, therefore the combined wavefront is flat and continuously changing with time, enabling dynamic beam steering. The time-dependent steering angle can be derived from the far-field expression, similar to the phased array case. Alternatively, considering that the phase difference between the emitters is $\Delta\omega t$ at a time constant t, substituting $\Delta\alpha$ in Eqn. 1.3 yields

$$\sin\theta = \frac{\Delta\omega t + 2m\pi}{k_0 d} \qquad m \in \mathbb{Z} \tag{1.4}$$

It shows that the steering angle varies with time without external control and the angular steering speed is proportional to the frequency gradient.

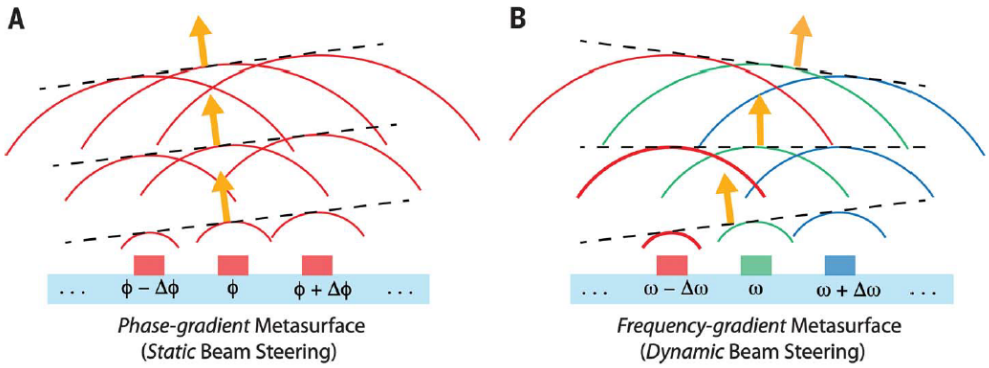

Figure 1.4. Schematic of (a) a phase-gradient metasurface and (b) a frequency gradient metasurface

In this thesis, we present an experimental demonstration of dynamic spatio-temporal steering of high repetition rate pulse trains using a spatial array of frequency combs with a uniform gradient in their carrier-envelope offsets (CEO), as proposed in [13]. Here, we provide the theoretical framework and proof-of-concept simulations, which were described in detail in [13].

Consider a spatial array of emitters separated by distance d, as illustrated in Figure. 1.5 (a). Each emitter is a cylindrical source extending along the z-axis, with the nth source located at $\vec{r_n}$ in the x-y plane. Each emitter emits an optical frequency comb with an identical spectral envelope and free spectral range (FSR), but there exists a uniform gradient in their carrier-envelope offsets across the emitter array, as shown in Figure. 1.5 (b). Assuming 2N+1

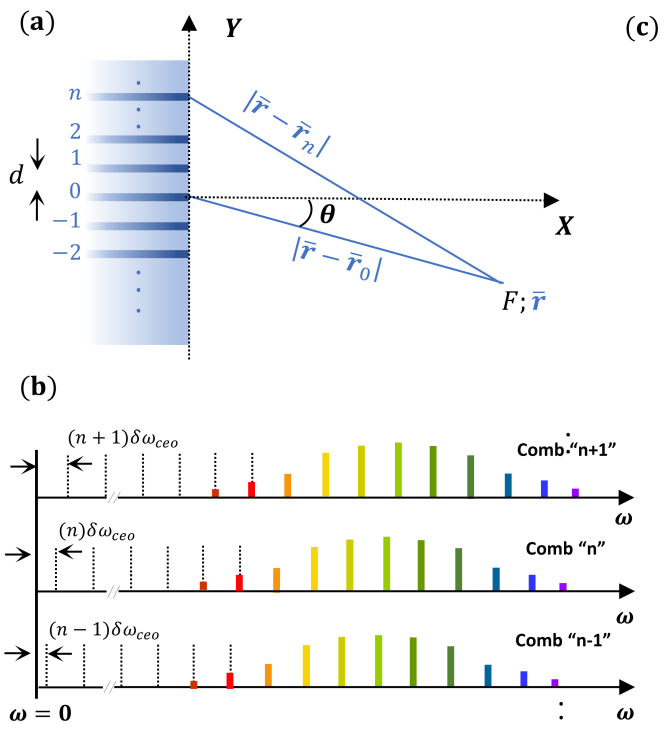

Figure 1.5. (a) Schematic of a uniform spatial array of sources spaced by d, (b) emitting optical frequency combs with a uniform gradient in their carrier-envelope offsets. [13]

emitters, each having 2M+1 spectral lines of amplitude A_m and an FSR of ω_{FSR}, with an increment in offset frequency between consecutive combs of $\delta\omega_{CEO}$, the effective electric field at a point F (denoted by vector $\vec{r}$ from the origin and angle θ from the x-axis) is given by

$$E(t,\vec{r}) = Re\left\{\sum_{n=-N}^{N}\sum_{m=-M}^{M}\frac{1}{\sqrt{|\vec{r}-\vec{r}_n|}}A_m \exp\left(\mathrm{j}\omega_{mn}t - \mathrm{j}k_{mn}|\vec{r}-\vec{r}_n|\right)\right\} \tag{1.5}$$

$$\omega_{mn} = \omega_0 + n\delta\omega_{CEO} + m\omega_{FSR},\ \ k_{mn} = \omega_{mn}/c$$

where ω_0 represents the center frequency of the frequency comb emitter $n = 0$, and c is the speed of light in free space.

At the far field, the distance $|\vec{r}-\vec{r_n}|$ between the source and the point F can be approximated as $R + nd\sin\theta$, where $|\vec{r}-\vec{r_0}| = R$. Substituting this approximation into the field expression, we obtain

$$E(t,R,\theta) = \frac{1}{\sqrt{R}}\mathrm{Re}\Big\{\sum_{m=-M}^{M} A_m \exp\Big(\mathrm{j}(\omega_0 + m\omega_{FSR})(t-\frac{R}{c})\Big) \sum_{n=-N}^{N} \exp\Big(\mathrm{j}n\delta\omega_{CEO}(t-\frac{R}{c}) - \mathrm{j}\frac{nd\sin\theta}{c}\omega_0 - \mathrm{j}\chi_{mn}\Big)\Big\} \tag{1.6}$$

$$\chi_{mn} = \frac{nd\sin\theta}{c}(n\delta\omega_{CEO} + \omega_{FSR})$$

When the parameters are chosen such that the χ_{MN} term is negligible compared to π, the field expression reveals two significant aspects. Firstly, the first summation represents the frequency comb source at $n = 0$, demonstrating a temporal pulsing rate of ω_{FSR}. Secondly, the second summation term describes the spatio-temporal steering of the pulses, with the time-dependent steering angle given by

$$\sin\theta = \frac{\delta\omega_{CEO}c(t-\frac{R}{c}) - 2\pi pc}{\omega_0 d} \qquad p \in \mathbb{Z} \tag{1.7}$$

This expression shows that the steering speed at a fixed range is proportional to the gradient in the CEO frequency. The angular scanning rate is $\delta\omega_{CEO}$ when the source separation d is half of the center wavelength of the $n = 0$ comb, i.e. $\lambda_0/2 = \pi c\omega_0^{-1}$.

To validate the theoretical framework, numerical simulations based on Eqn. 1.5 were conducted. The simulation involves 41 frequency combs spaced by half of the center wavelength, each containing 9 spectral lines. Each comb is characterized by a Gaussian spectral envelope with a -10 dB bandwidth of $\sim$ 180 GHz. The FSR is set to 60 GHz, and the frequency gradient across the comb array is set to 10 GHz. Figure. 1.6 shows the normalized electric field intensity as a function of time and angle θ, at a range of 15 mm from the origin. The angular scanning period is 100 ps, corresponding to the inverse of the increment in CEO frequency. The repetition period of the pulses is $\sim$ 16.7 ps, corresponding to the inverse of the FSR. As a result, six pulses are emitted in one steering cycle. The steering angle vs. time follows a sine inverse relation, as expected in Eqn. 1.7.

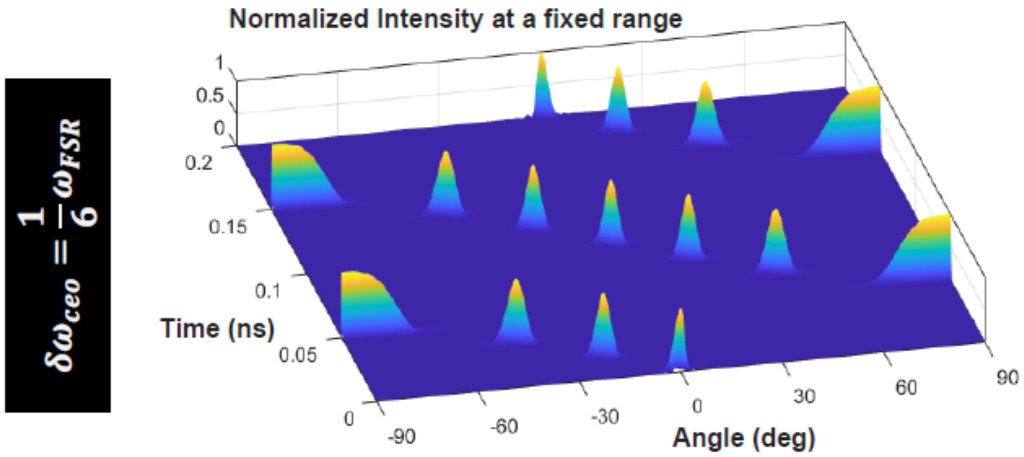

Figure 1.6. Normalized electric field intensity as a function of time and angle θ, at a range of 15 mm from the origin [13]

Figure. 1.7 illustrates the normalized electric field intensity in the x-y plane at two different instants of time separated by 3 pulse repetition periods, $3 \times 2\pi\omega_{FSR}^{-1}$. The decay from beam divergence is excluded. The radial grid lines are uniformly spaced at a distance equivalent to the distance traveled by light during one repetition period. Six pulses are numbered to track their propagation after 3 repetition periods. It shows that one pulse is emitted from the origin during each repetition cycle, resulting in three additional pulses emitted after 3 cycles. The steering direction changes from the direction of the 5th pulse to that of the 2nd pulse. After emission, each pulse continues to propagate radially at its initially emitted steering angle. Hence, the numbered pulses can be seen traveling across 3 grid lengths in 3 repetition periods. In summary, the presented scheme demonstrates dynamic pulsed beam steering, with discrete temporal and spatial scanning steps determined by the FSR and the frequency gradient of the spatial array of combs.

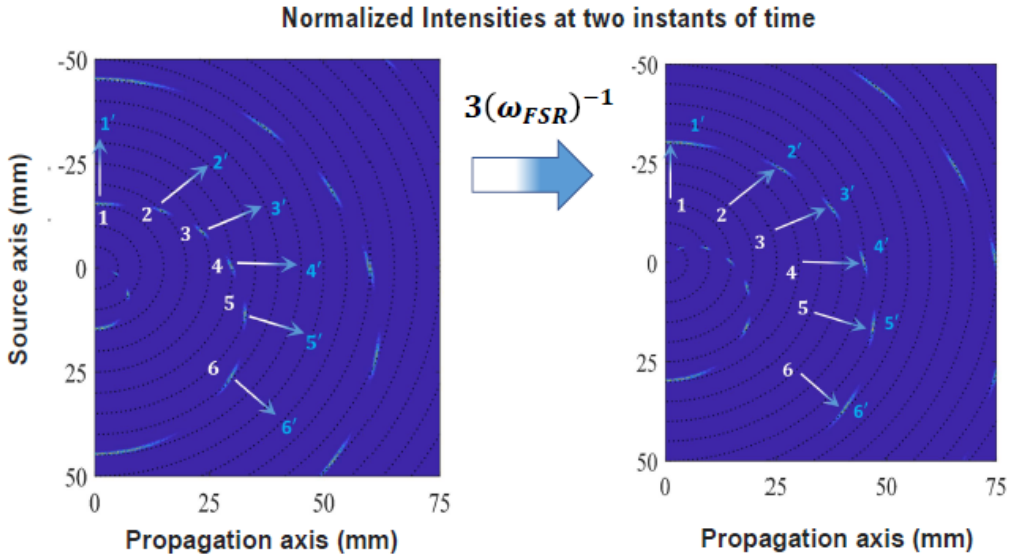

Figure 1.7. Normalized electric field intensity in the x-y plane at two different instants of time separated by 3 pulse repetition periods. [13]

1.2 Virtually Imaged Phased Array

We used a virtually imaged phased array (VIPA) [14] to generate the spatial array of frequency combs. The VIPA is a side-entrance Fabry-Perot etalon that functions as a spectral disperser. Due to its large angular dispersion and high efficiency, VIPAs have been used in wavelength-division multiplexing (WDM) [15], [16], pulse shaping [17], optical spectroscopy [18], [19] and frequency-modulated continuous-wave (FMCW) LiDAR [20].

As shown in Figure. 1.8, the VIPA consists of two glass plates separated by either air or some glass material of refractive index n_r and is referred to as air VIPA and solid VIPA respectively. The front plate is nearly 100% reflective, except for an uncoated or anti-reflection coated window area. The back plate is partially reflective with a reflectivity typically larger than 95%. The input beam is focused into the VIPA by a cylindrical lens through the window area at a small input angle, then bounces back and forth between the two plates, producing multiple reflections on the back plate. As indicated by the name virtually imaged phased array, the multiple reflections form as if they diverge from an array of virtual images spaced from their corresponding reflection spots by a distance L, which equals the distance that the

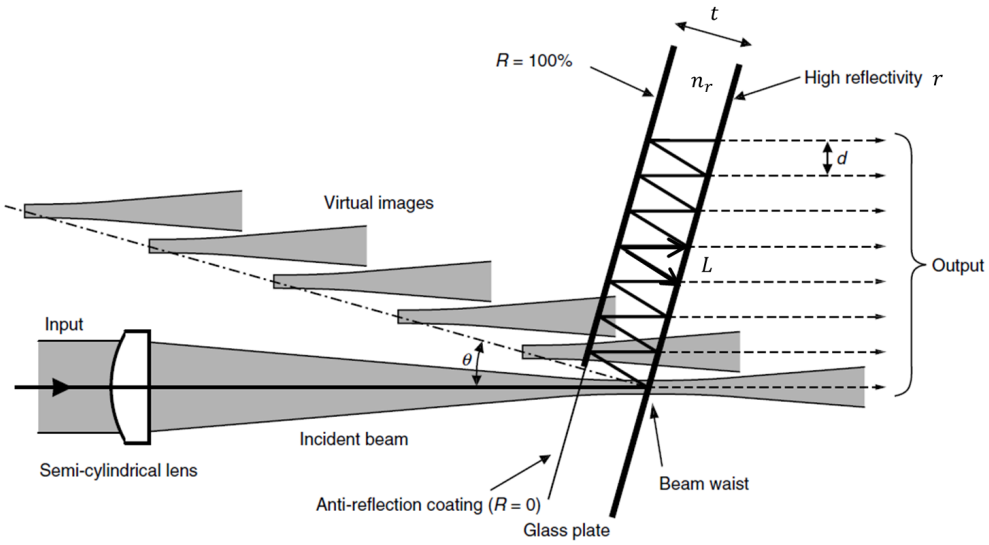

Figure 1.8. Structure of VIPA in side view. Adapted from [21].

beam traveled between two reflections. Since this phase difference is frequency-dependent, similar to a diffraction grating, the interference of the array of multiple reflections leads to angular dispersion. As in Fabry-Perot etalons, VIPA has an FSR determined by the optical path length $n_r L$ between two reflections. Consequently, for a broadband input, frequencies separated by the VIPA FSR will be directed to the same angle and spatial position on the Fourier plane. This posed a problem for some applications since the total dispersion bandwidth is limited by the VIPA FSR (typically a few hundred GHz), and was resolved by using another broadband disperser along the orthogonal axis [17], [18]. However, this feature is crucial for our experiments.

The dispersion behavior of VIPA has been fully studied by Xiao *et al* in [22], [23] based on paraxial wave theory. They obtained the intensity distribution on the Fourier plane (see Figure. 1.9) of VIPA by assuming a Gaussian input beam and summing over the field of virtual sources after spatial Fourier transform by a thin lens. For an air VIPA, the resulting intensity expression is

$$I_{out}(x_F, \lambda) \propto \exp(-\frac{\pi^2 w_0^2}{\lambda_0^2}\frac{x_F^2}{F^2}) \times \frac{1}{(1-Rr)^2 + 4Rr\sin(k\Delta/2)^2} \tag{1.8}$$

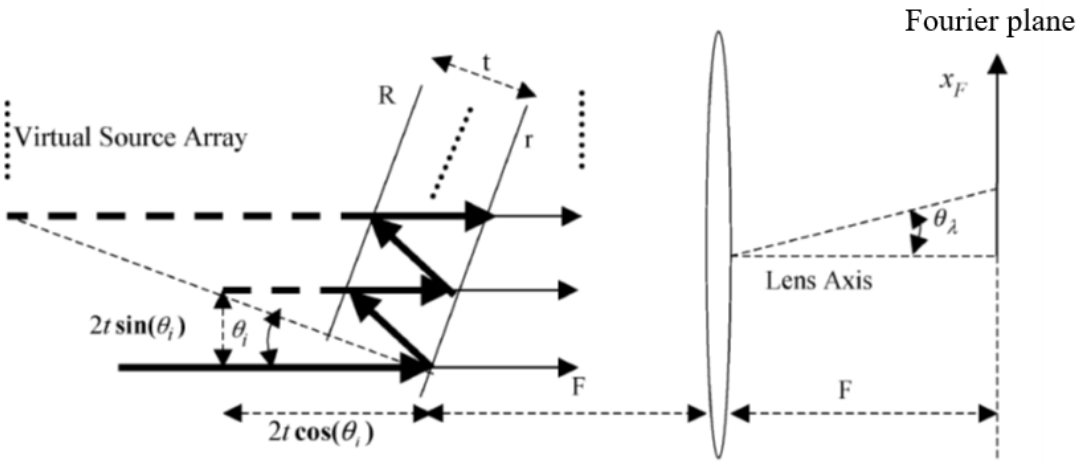

Figure 1.9. VIPA geometry, showing the virtual source array, multiple reflections, and the Fourier plane. Adapted from [22].

where $\Delta = 2t\cos\theta_{\mathrm{i}} - \frac{2t\sin\theta_{\mathrm{i}}}{F} - \frac{t\cos\theta_{\mathrm{i}}x_F^2}{F^2}$, w_0 is the beam waist of the input beam, F is the focal length of the lens, R and r are the reflectivities of the two plates of the VIPA, θ_{i} is the input angle, t is the thickness of VIPA. For a fixed wavelength, the spatial intensity distribution follows a Gaussian distribution envelope characterized by the input beam waist. At a fixed position x_F, the transmission spectrum exhibits an Airy-Lorentzian lineshape and the transmission peaks satisfy the constructive interference condition $k\Delta = 2m\pi$, which is the dispersion law of VIPA:

$$k(2t\cos\theta_{\mathrm{i}} - \frac{2t\sin\theta_{\mathrm{i}}}{F} - \frac{t\cos\theta_{\mathrm{i}}x_F^2}{F^2}) = 2m\pi \tag{1.9}$$

From this dispersion law, the VIPA FSR at a specific x_F is given by

$$FSR = \frac{c}{2t\cos\theta_{\mathrm{i}} - \frac{2t\sin\theta_{\mathrm{i}}}{F} - \frac{t\cos\theta_{\mathrm{i}}x_F^2}{F^2})} \tag{1.10}$$

It shows that FSR varies slightly with changes in the input angle and along x_F axis of the Fourier plane. The theoretically minimal FWHM bandwidth in wavelength is given by (at $x_F = 0$)

$$FWHM = \frac{\lambda_0^2}{2\pi t \cos\theta_{\mathrm{i}}} \frac{1 - Rr}{\sqrt{Rr}} \tag{1.11}$$

FWHM can be improved by increasing Rr. The measured linewidth in practice can be several times larger due to the limited number of reflections. So the linewidth is narrower at small input angles since there are more reflections. The relation between the peak wavelength and output angle $\theta_\lambda \approx x_F/F$ is derived as

$$\Delta\lambda = \lambda_p - \lambda_0 = -\lambda_0[\tan(\theta_{\mathrm{i}})\theta_\lambda + \frac{1}{2}\theta_\lambda^2] \tag{1.12}$$

Which demonstrates a quadratic dependence on the output angle. Using this expression, one can measure the spectra at different output angles and determine the input angle by fitting the data, the exact value of which is difficult to directly measure in experiments and is useful for other analyses.

Using a frequency comb source as input, the individual comb lines will be directed to different positions on the Fourier plane based on the dispersion law. If the comb spacing matches the VIPA FSR, subsets of comb lines separated by VIPA FSR will overlap at the same position and there is an offset frequency shift between adjacent subsets. This is illustrated in Figure. 1.10, which shows a 2D image of the Fourier plane using a VIPA and a diffraction grating together in a cross-dispersion configuration, where different subsets of comb lines are later separated again by the grating.

For our experiments, we are more interested in the output plane profile of VIPA since we expect to observe beam steering behavior on this plane. Shirasaki *et al* [14], [24] proposed a model of the VIPA that calculates the output profile by summing up the field of the multiple reflections $T(x) = \sum_{\mathrm{i}} E_{\mathrm{i}}(x)$, where T(x) is the transmissivity of the back plate of VIPA along the x-axis and $E_{\mathrm{i}}(x)$ is the field of the ith reflection, calculated using Gaussian beam propagation and reflectivity. Their simulation for the uniform reflectivity case demonstrated an approximately exponential profile for the back plane and a corresponding Lorentzian

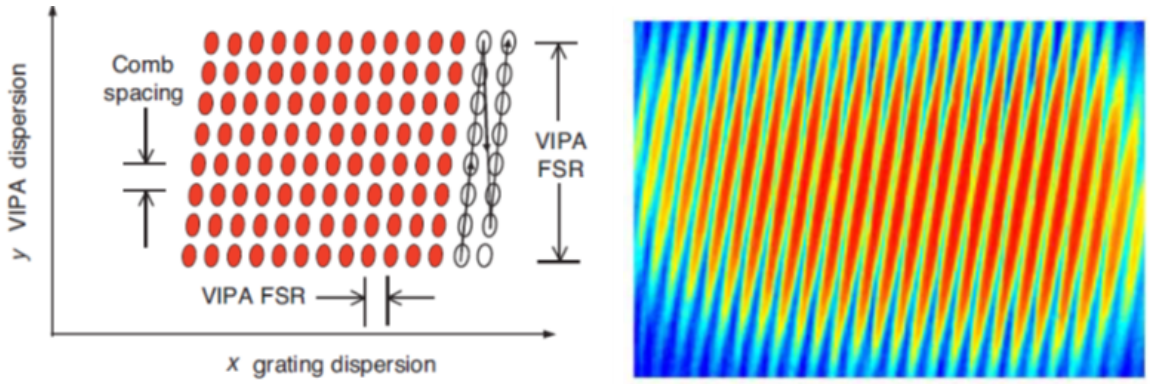

Figure 1.10. Left: Within each column (VIPA dispersion axis), the beam spots are separated by the frequency comb spacing; Within each row (grating dispersion axis), the beam spots are separated by the VIPA FSR. [18] Right: A 2D image of the Fourier plane for a 50 MHz fiber laser input into a 200 GHz VIPA. Discrete dots are not shown along the VIPA dispersion axis due to limited spectral resolution. [17]

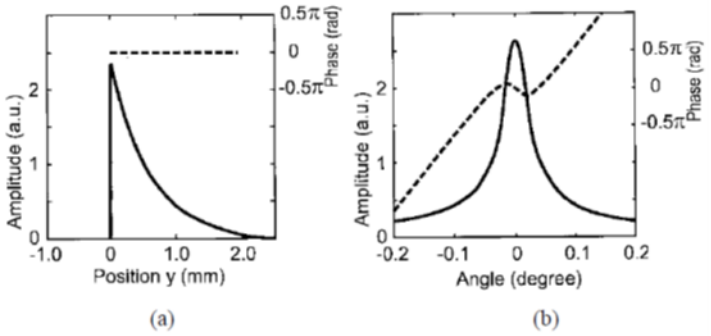

Figure 1.11. (a) Output beam profile and (b) Fourier plane profile. Solid line: Amplitude; Dashed line: Phase. [21]

profile for the Fourier plane (see Figure. 1.11). The simulation was conducted under the following conditions: $t = 100\ \mu m$, $n_r = 1.5$, $\theta_{\mathrm{i}} = 4.3°$, $w_0 = 5.7\ \mu m$, and $Rr = 95\%$. Then they presented simulation results for a graded reflectivity design, which yielded a Gaussian-like profile for the Fourier plane. So the new design is expected to improve mode coupling efficiency into the fiber and reduce cross-talk. Later research [23] analyzed a Fourier plane profile sharper than the Lorentzian distribution (see Eqn. 1.8 for a fixed wavelength).

1.3 Outline

The thesis is organized as follows. Chapter 2 will focus on the generation of the spatial array of frequency combs, emphasizing a uniform gradient in their offset frequencies. Chapter 3 will focus on the investigation of the far field pattern of this comb array and demonstrate dynamic pulsed beam steering.

2. GENERATION OF A SPATIAL ARRAY OF FREQUENCY COMBS WITH A FREQUENCY GRADIENT

2.1 Characterization of VIPA

In this section, we will utilize the dispersion law described in Section. 1.2 to characterize the VIPA used in our experiments. The characterization method is described in detail in [22]. Specifically, we investigated the dispersion behavior of our VIPA by using a broadband source as input and measuring the spectra at different spatial positions on its Fourier plane. By fitting the spectral data with the dispersion law, we determined the values of the focal length and the incident angle. The characterization experiments help us test the performance of our VIPA device, understand the spatial distribution of frequency comb lines, and provide useful information for determining the temporal delay in our beam steering experiments.

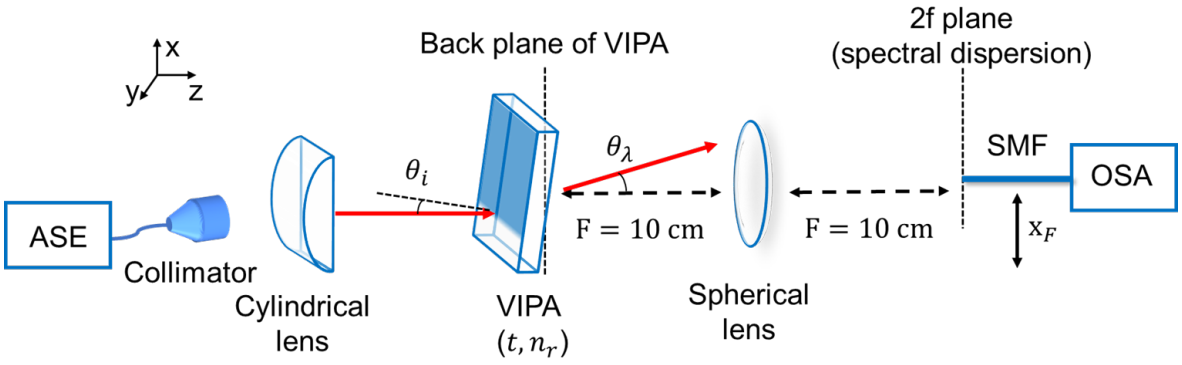

Figure 2.1. Experimental setup for VIPA characterization. [22]

The VIPA used in our experiments is a solid VIPA with a nominal thickness (t) of 1.5 mm and a nominal refractivity (n_r) of 2, which corresponds to a 50 GHz FSR. The experimental setup for characterizing the VIPA is shown in Figure. 2.1. In this setup, the input source is an amplified stimulated emission (ASE) source with a bandwidth ranging from 1530 nm to 1570 nm. The collimated beam from the input source is focused into the VIPA by a cylindrical lens. For precise control of the incident angle, the VIPA is mounted on a fine rotational stage. A spherical lens with a focal length of $F = 10$ cm focuses light from different output angles onto different positions on its back focal plane. To capture the spectra, a single-mode

fiber connected to an optical spectrum analyzer (OSA) is scanned along the x-axis on the back focal plane.

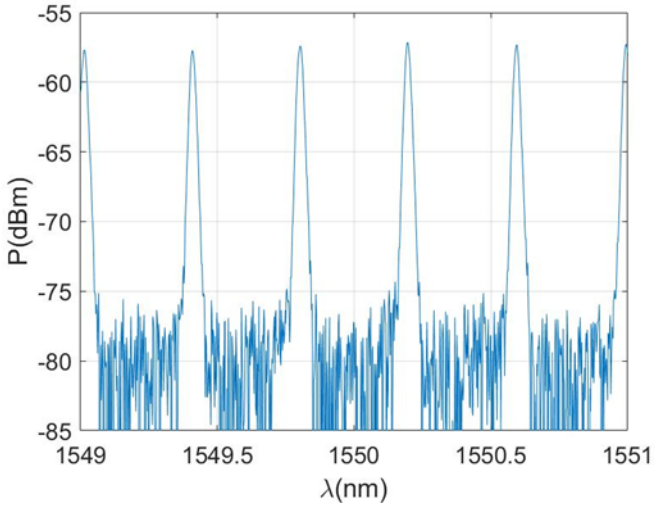

Figure 2.2. A spectrum measured at the Fourier plane of VIPA

An example of the output spectrum is presented in Figure. 2.2. It shows multiple peak intensities separated by approximately 0.4 nm, in accordance with the nominal 50 GHz FSR. The FWHM of the peaks is measured to be approximately 0.02 nm, which is comparable to the resolution of the OSA used in the experiment, while the theoretical minimum FWHM is calculated to be $\sim 5\ pm$. The position of the fiber is carefully adjusted to be on the Fourier plane to prevent any broadening and asymmetry caused by the spatial chirp effect [23]. Then we found the peak output wavelengths at different spatial positions from the spectra and fit them using the dispersion law. The dispersion law for a solid VIPA is [22]:

$$\Delta\lambda = \lambda_p - \lambda_0 = -\lambda_0[\frac{\tan(\theta_{in})\cos(\theta_i)}{n_r\cos(\theta_{in})}\theta_\lambda + \frac{1}{2n_r^2}\theta_\lambda^2] \tag{2.1}$$

Where θ_λ is the output angle, $x_F \approx \theta_\lambda F$ is the output position along the dispersion axis on the Fourier plane, θ_i is the incident angle, θ_{in} is the internal angle inside VIPA and $\sin(\theta_i) = n_r\sin(\theta_{in})$. The equation can be rewritten as:

$$\lambda_p = -\frac{\lambda_0}{2n_r^2F^2}x_F^2 - \frac{\tan(\theta_{in})\cos(\theta_i)}{n_r\cos(\theta_{in})}\frac{\lambda_0}{F}x_F + \lambda_0 \tag{2.2}$$

we fit a second-order polynomial to the collected data and obtain the focal length of the spherical lens and the incident angle. The zero x_F position is identified by finding the position with maximum output power. Figure. 2.3 and 2.4 present two sets of dispersion data obtained at different incident angles. In both figures, the experimental data points are represented by circles, while the fitting results are shown as lines. The spectra were measured with a step length of 0.2 mm within a range of $2 \sim 3$ mm. For the data in Figure. 2.3, the average fitted value for the focal length is 9.97 cm, which closely aligns with the nominal value of 10 cm. This agreement supports the reliability of the refractivity value of VIPA. The average fitted incident angle is found to be 2.08 degrees. In Figure. 2.4, the fitted value for the focal length is 10.11 cm (for the center line), again in close agreement with the nominal value of 10 cm. The fitted incident angle is 7.56 degrees. At larger incident angles, the slope of the wavelength versus position becomes steeper, corresponding to a smaller angular dispersion, and the linear term dominates over the quadratic term as indicated in the dispersion equation.

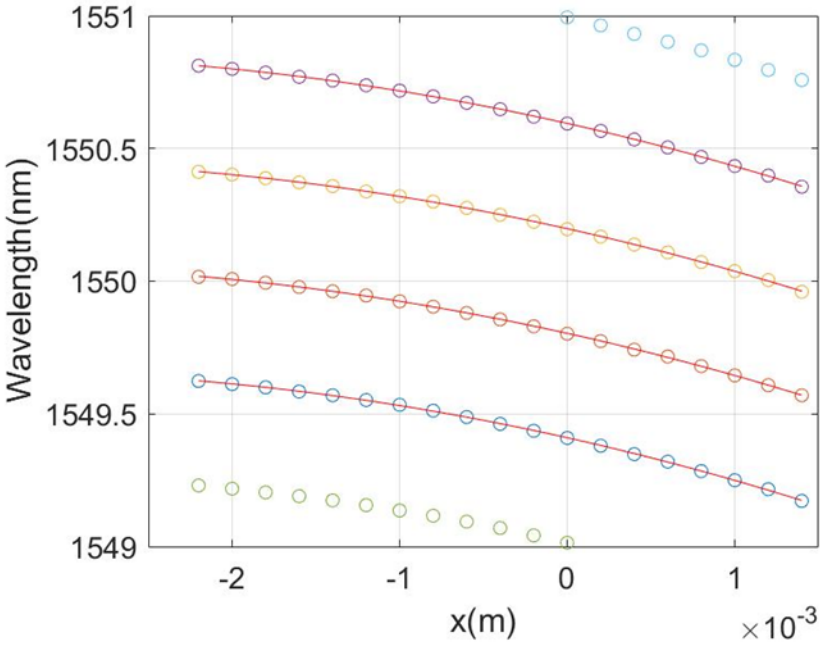

Figure 2.3. Dispersion data for a fitted incident angle of 2.08°

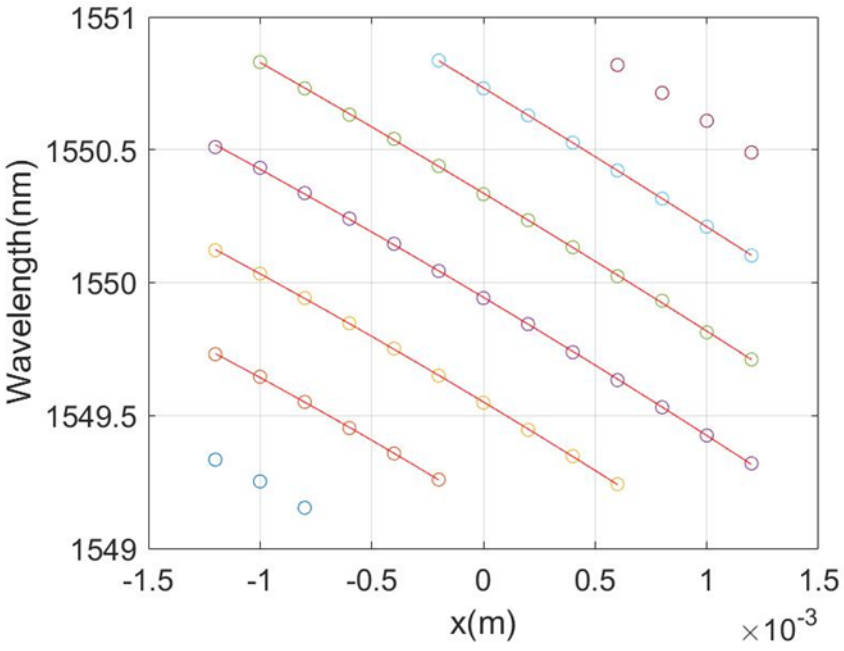

Figure 2.4. Dispersion data for a fitted incident angle of 7.56°

2.2 Electro-optic Comb

We used an electro-optic comb (EO comb) as the input frequency comb source. The details of this EO comb can be found in [25].

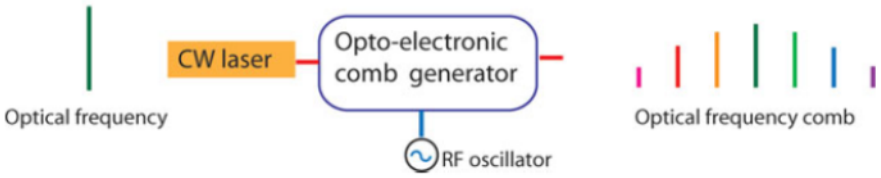

Figure 2.5. General layout of an EO comb generator. [26]

EO combs offer several advantages, including a relatively high repetition rate, high sideband power, simplicity, and independent tunability of the repetition rate and central frequency [26]. These characteristics enable us to achieve a high and flexible temporal pulsing rate in our beam steering experiments. The generation of EO combs involves the electro-optic modulation of a CW laser, resulting in equally spaced sidebands around the carrier frequency. The general scheme for EO comb generation is illustrated in Figure. 2.5. The center frequency and frequency spacing of the comb can be tuned independently by adjusting the frequency of the CW laser and the RF oscillator that drives the modulators.

The EO comb used in our experiments can achieve a flat spectrum consisting of 60-75 comb lines within a -10 dB bandwidth, covering a 6-18 GHz spacing tuning range. This allows us to divide it into more than 5 frequency combs, each comprising $\sim$ 8 comb lines and with a relatively uniform power distribution. The layout of the EO comb is shown in Figure. 2.6. It consists of three phase modulators (PMs) and one intensity modulator (IM), all driven by the same RF oscillator. The IM ($V_\pi \sim 5.5$ V at 10 GHz) is used to generate a pseudo-square pulse train by appropriately adjusting its bias. Three PMs are cascaded to achieve a broad spectrum. Each PM has $V_\pi \sim 3.5$ V at 10 GHz and can handle a maximum RF power of 1 W, hence adding more than 20 lines within -10 dB bandwidth. If the flat-top pulse train only carves the modulated light where the chirping provided by the PMs is almost linear, a relatively flat spectrum can be obtained. The chirp from the PMs

is correctly aligned by selectively activating each PM using the RF switch and adjusting the phase of the driving signal with the phase shifter sequentially. Additionally, low-pass filters are employed to eliminate the second harmonic signal from the RF amplifiers when operating at low repetition rates (below 11 GHz).

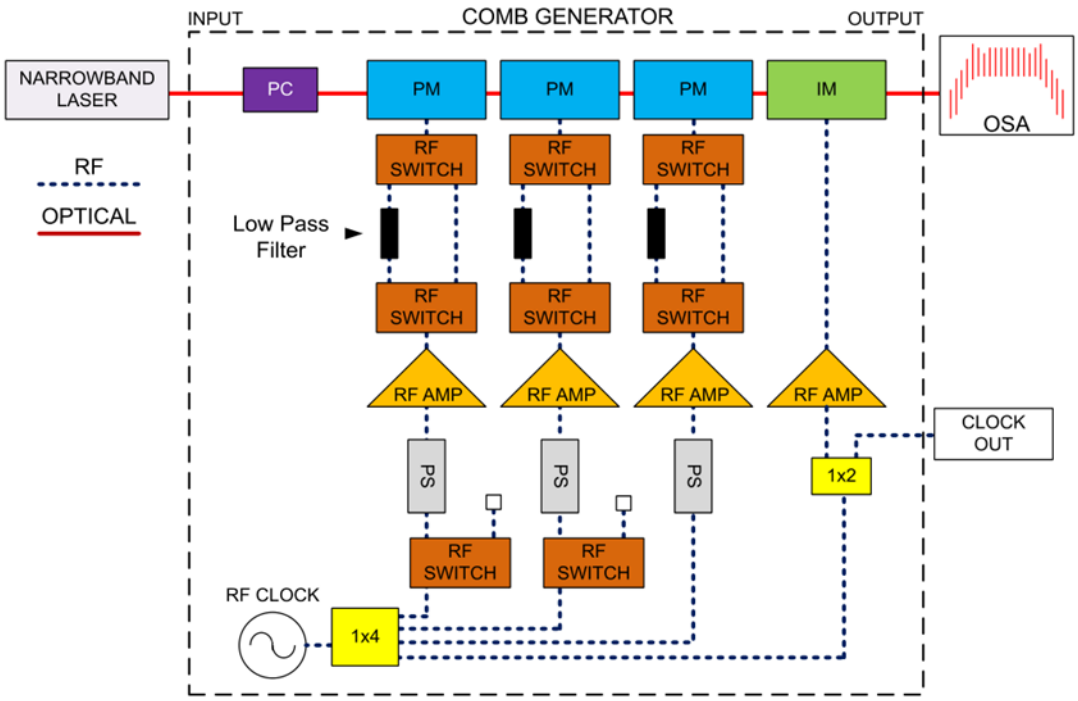

Figure 2.6. Layout of the EO comb. PC, polarization controller, RF AMP, RF amplifier, PS, phase shifter. [25]

The spectral flattening process can be explained in terms of time-to-frequency mapping (Figure. 2.7). [27], [28] The sinusoidal phase modulation provided by the PMs can be approximated as a quadratic function at its peaks or valleys. This quadratic phase modulation is known as a time lensing effect, which bears an analogy to the effect of a thin lens on a spatial beam. When the chirping rate is sufficiently high, the resulting spectral envelope takes the shape of the temporal envelope of the input pulse, thereby achieving time-to-frequency

conversion. Assume a single input pulse $c(t)/C(\omega)$ and a time lens with a quadratic phase modulation function $m(t)/M(\omega)$

$$m(t) \propto \exp(\mathrm{j}\frac{\ddot{\phi}_t}{2}t^2), \quad M(\omega) \propto \exp(-\mathrm{j}\frac{1}{2\ddot{\phi}_t}\omega^2) \tag{2.3}$$

The spectrum of the output pulse from the time lens is given by

$$\begin{aligned} D(\omega) &= C(\omega) * M(\omega) \\ &\propto \int_{\Delta\omega} C(\Omega)\exp(-\mathrm{j}\frac{1}{2\ddot{\phi}_t}(\omega-\Omega)^2)d\Omega \\ &\propto M(\omega)\int_{\Delta\omega} C(\Omega)\exp(-\mathrm{j}\frac{1}{2\ddot{\phi}_t}\Omega^2)\exp(\mathrm{j}\frac{1}{\ddot{\phi}_t}\omega\Omega)d\Omega \end{aligned} \tag{2.4}$$

Where $\Delta\omega$ is the bandwidth of the input pulse. If the chirp is large enough such that

$$|\ddot{\phi}_t| \gg \frac{\Delta\omega^2}{8\pi} \tag{2.5}$$

the first phase term $\exp(-\mathrm{j}\frac{1}{2\ddot{\phi}_t}\Omega^2)$ can be neglected as $\frac{1}{2\ddot{\phi}_t}\Omega^2 < \frac{1}{2\ddot{\phi}_t}(\frac{\Delta\omega}{2})^2 \ll \pi$. Then the spectrum function can be approximated as

$$D(\omega) \propto M(\omega)\int_{\Delta\omega} C(\Omega)\exp(\mathrm{j}\frac{1}{\ddot{\phi}_t}\omega\Omega)d\Omega = M(\omega)c(t=\frac{\omega}{\ddot{\phi}_t}) \tag{2.6}$$

This equation demonstrates that when the inequality condition is satisfied, the output spectral envelope is proportional to the temporal waveform of the input pulse, with a quadratic phase factor $M(\omega)$. In our case, the pseudo-square pulse train generated by the IM can be mapped into a flat-top spectrum (Figure. 2.8). The "rabbit ear" structure, which is commonly observed at the outer part of the spectrum, is due to the deviation of the sinusoidal phase modulation from the quadratic function at the edges of the flat-top input pulses, where the instantaneous frequency is close to the minimum or maximum values.

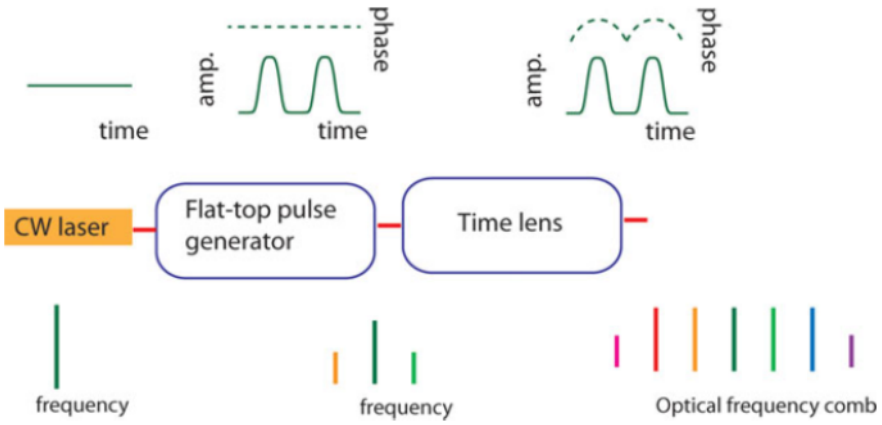

Figure 2.7. General layout for flat comb EO comb generation based on time-to-frequency mapping. [26]

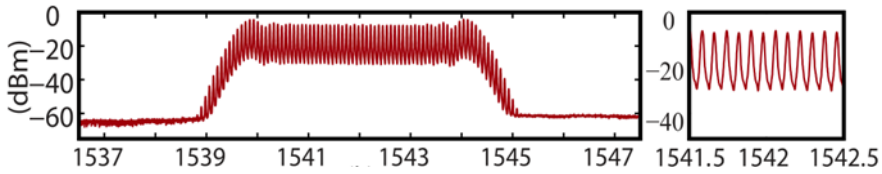

Figure 2.8. An output comb spectrum with 10 GHz repetition rate and 65 lines within -10 dB. [25]

The EO comb can be compressed to its bandwidth-limited duration, which indicates a high spectral coherence. The compression is performed via line-to-line pulse shaping by compensating the spectral phase in an iterative manner, aiming to optimize the autocorrelation trace. The compression results for a comb with a repetition rate of 12 GHz are shown in Figure. 2.9. The autocorrelation trace of the compressed pulse closely resembled the transform-limited case, which was calculated from the measured spectrum assuming a constant spectral phase. Although the applied phase was optimized up to the eighth order, it was actually nearly quadratic, as discussed earlier.

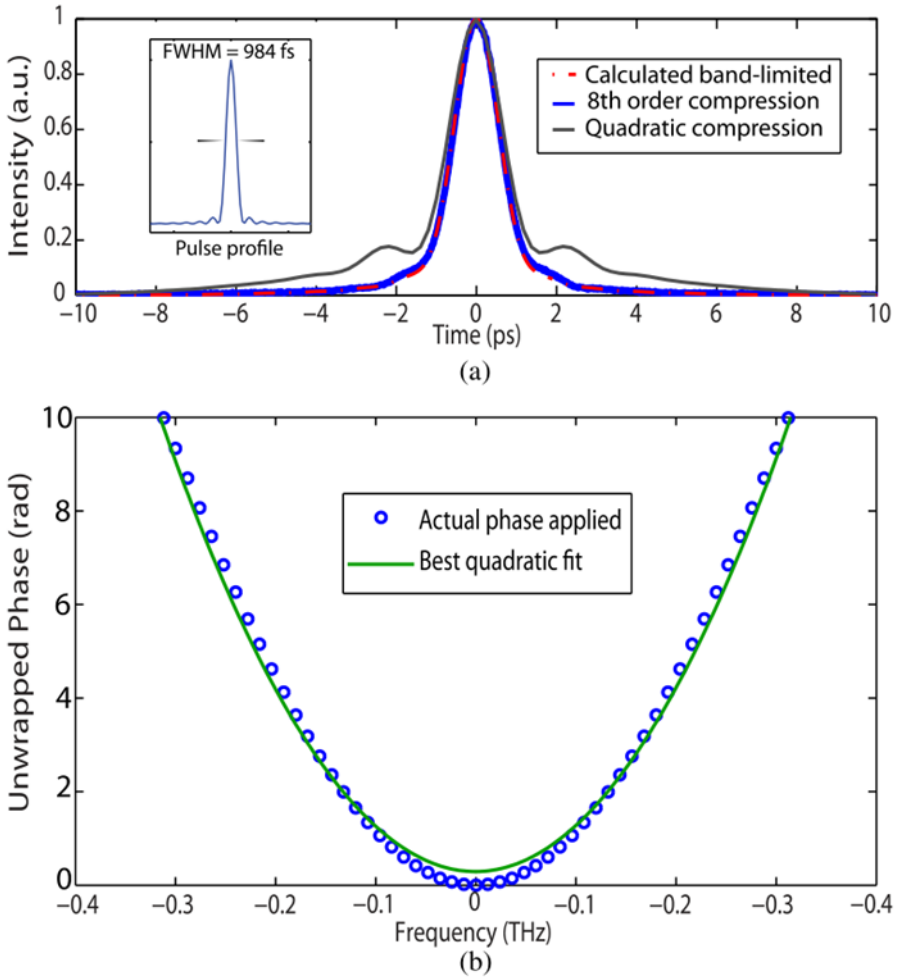

Figure 2.9. (a) Red dashed line: Calculated autocorrelation trace for bandwidth limited case. Blue line: Measured autocorrelation trace corrected up to 8th order. Gray line: Calculated autocorrelation trace using only quadratic phase. (b) Actual applied phase and its best quadratic fit. [25]

2.3 Experimental Results

In this section, we will present the results of generating an array of frequency combs using the EO comb described in the previous section.

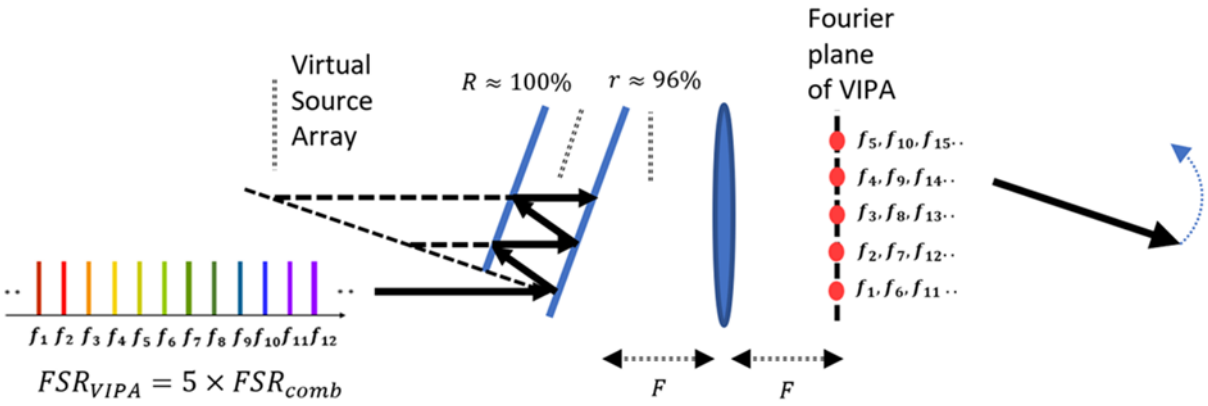

Figure 2.10. Diagram of the experimental setup

The experimental setup remains the same as the characterization experiments but with the EO comb source as the input. As explained in section 1.2, the individual comb lines of the input comb will be directed to different positions on the Fourier plane based on the dispersion law. When the comb FSR precisely matches an integer fraction of the VIPA FSR, subsets of comb lines separated by the VIPA FSR will superimpose on each other. Furthermore, there will be an offset frequency shift equal to the value of the comb repetition rate between adjacent subsets. This is illustrated in Figure. 2.10.

Given that the VIPA FSR is approximately 50 GHz and the EO combs spacing tuning range spans from 6 GHz to 18 GHz, we chose to set the comb repetition rate to roughly 10 GHz, which is one-fifth of the VIPA FSR. Utilizing the dispersion data presented in Section 2.1, the average FSR is calculated to be $\sim$ 49.3 GHz for an incident angle of 7.56 degrees at a wavelength of 1550 nm. Taking into account the zero offset frequency of the RF oscillator, we fine-tuned the comb FSR around 9.7-10 GHz to optimize the oscillation frequency such that each set of comb lines overlapped at the same position. Then we determined the RF oscillator frequency to be 9.84 GHz and set up the EO comb following the procedures in [25] to achieve a flat spectrum. Figure. 2.11 shows the measured comb

spectrum, which contains ~ 50 comb lines within a -10 dB bandwidth, and the average comb spacing is measured to be 9.85 GHz.

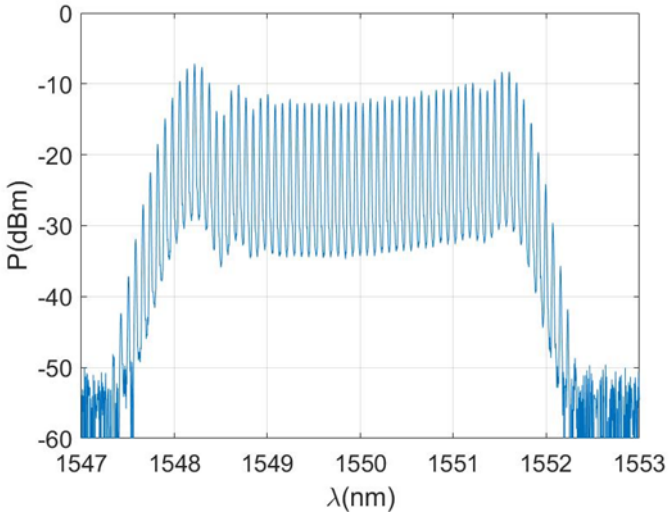

Figure 2.11. Spectrum of the input EO comb

We input the EO comb source to our VIPA setup and measured the spectra while scanning the single-mode fiber (SMF) along the dispersion axis (x-axis) on the Fourier plane. The translation stage used for scanning has a resolution of 0.01 mm, and the mode diameter of the SMF is also ~ 0.01 mm. The optical spectrum analyzer (OSA) utilized has a resolution of 0.02 nm (~ 2.5 GHz). The obtained results show a spatial distribution of distinct comb line sets. Figure. 2.12 displays a portion of the spectra measured along the x-axis with a step size of 0.01 mm. It demonstrates a spatial separation of ~ 0.15 mm and a frequency shift of ~ 9.8 GHz between the peak frequencies. The divided frequency combs are well separated with a noise power level between them, except for a -10 dB side lobe that is likely a result of slight misalignment in the setup. Figure. 2.13 plots the spectra of three adjacent frequency combs located near the center, each having an FSR of ~ 49.2 GHz, with a frequency shift of ~ 9.8 GHz between them. The power distribution of these comb lines resembles that of the input EO comb. Figure. 2.14 shows the spatial distribution of each comb line from the input EO comb. Each dot represents a frequency mode, and each row of dots is tilted according to the angular dispersion of VIPA. The dots are separated by a spatial spacing of 153 ± 9 μm, and the tilt corresponds to a frequency shift of 9.81 ± 0.07 GHz. Due to the

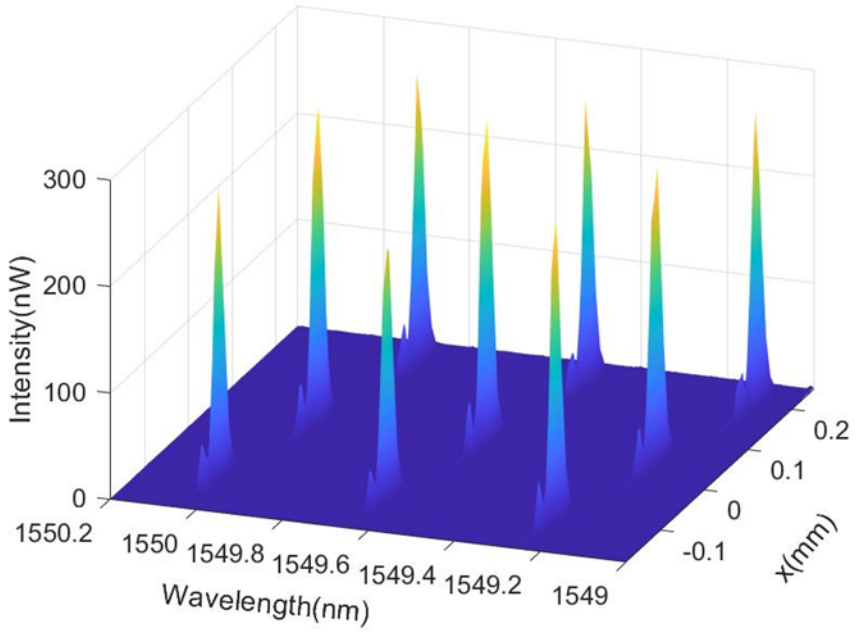

Figure 2.12. Spectral and spatial distribution of 9 frequency modes

relatively high incident angle on the VIPA, the frequency to space mapping is nearly linear, where 1mm along the dispersion axis yields a frequency shift of $\sim$ 6.4 GHz (0.5 nm), as expected from the dispersion data in Section 2.2. For each column, the separation represents the VIPA FSR, with a value of 49.16 ± 0.03 GHz. In the observed spatial range of ~ 2 mm, it is worth noting that although more than 10 frequency combs are visible, the ones falling outside the VIPA FSR (which corresponds to the diffraction orders of the same input comb mode) exhibit a power level that is over 3 dB lower.

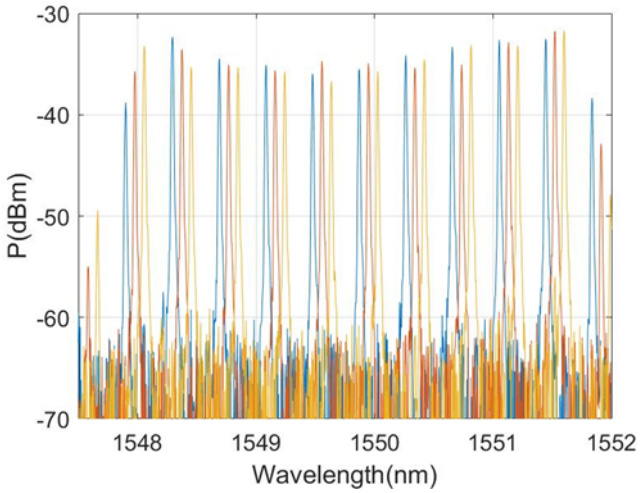

Figure 2.13. Spectra of three adjacent frequency combs

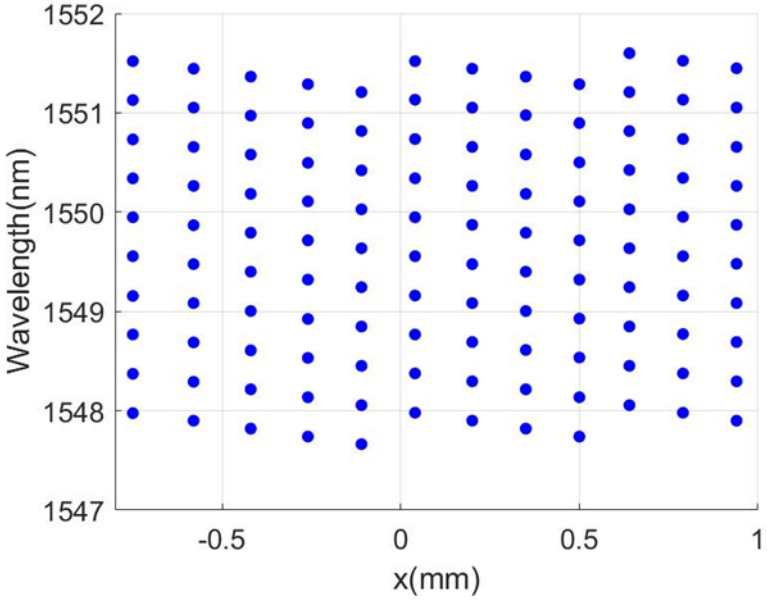

Figure 2.14. Spatial distribution of the comb teeth

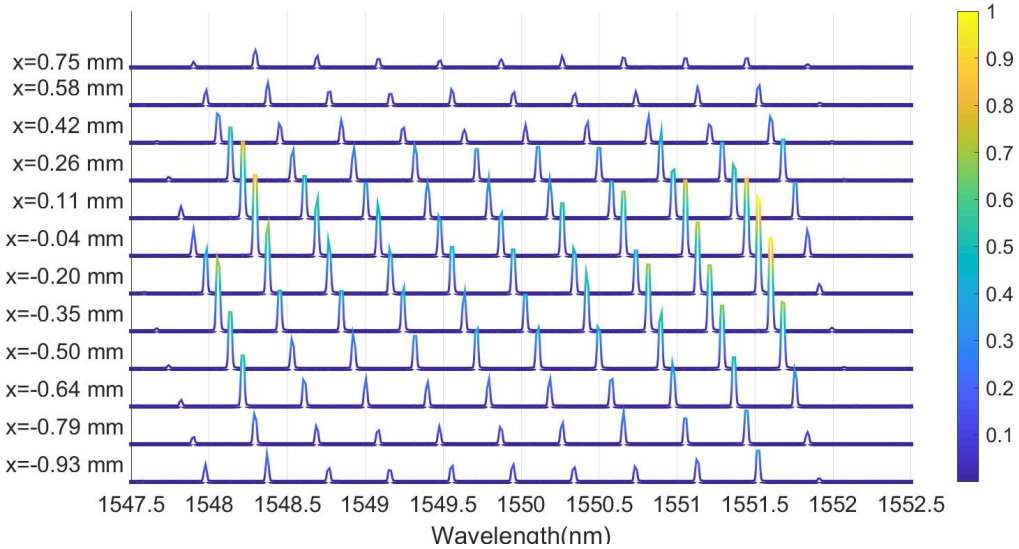

Figure 2.15. Spectra of the spatial array of frequency combs

3. EXPERIMENTAL RESULTS OF DYNAMIC PULSED BEAM STEERING

In Section 2.3, we presented the generation of a spatial array of frequency combs on the Fourier plane of the VIPA, showcasing a gradient in their carrier frequency offsets. In this chapter, we will explore the far-field pattern of this array by incorporating an additional lens after the Fourier plane. This will allow us to observe the pulsed beam steering behavior.

3.1 Experimental setup

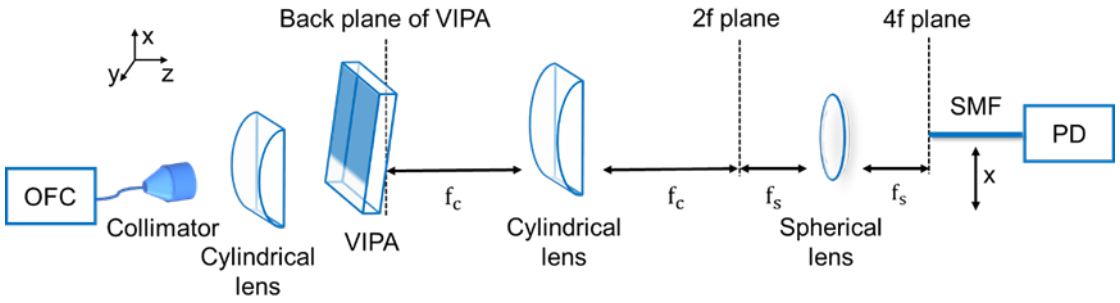

Figure 3.1. Experimental setup. OFC: optical frequency comb, VIPA: virtually imaged phased array, SMF: single-mode fiber.

The experimental setup is illustrated in Figure. 3.1. A frequency comb source is focused into the VIPA using a cylindrical lens with a focal length of 10 cm. The incident angle is found to be 7.56° by using the dispersion law of VIPA in Section 2.1. The output beam from the VIPA then undergoes frequency-to-space mapping by a cylindrical lens with a focal length f_c of ~ 6 cm, resulting in a spatial array of frequency-shifted spectra along the dispersion axis (x-axis) on the Fourier plane or the 2f plane. To examine the far-field pattern, a spherical lens with a focal length f_s of around 3.5 cm is introduced after the 2f plane. The lens maps the steering angle to a position on the x-axis at its Fourier plane or the 4f plane. Since the two lenses form a 4f imaging system, the 4f plane represents a scaled-down version of the VIPAs back plane, with a demagnification factor of ~ 0.58 along the x-axis. Along the y-axis, the collimated output beam from the VIPA is focused by the spherical lens. As explained in Section 1.2, the back plane of the VIPA comprises an array of delayed beams.

The delay corresponds to the separation of the virtual sources and can be measured using the VIPA FSR found in the 2f plane experiments. For our setup, we expect the delay to be around 20 ps due to the $\sim$ 50 GHz VIPA FSR. To observe the delayed beams, a single-mode fiber (SMF) connected to a 23 GHz photodetector (PD) is scanned along the x-axis in the 4f plane.

To validate the concept of dynamic pulsed beam steering using frequency gradient spectra, in Section 3.2, we employed a mode-locked fiber laser with a repetition rate of $\sim$ 50 MHz and a 3 dB bandwidth of $\sim$ 40 nm centered around 1590 nm as the input frequency comb source. Since the minimum theoretical resolution [23] of the VIPA is $\sim$ 5 pm/$\sim$ 600 MHz, which is much larger than the 50 MHz repetition rate of the mode-locked laser, the individual comb lines cannot be resolved on the 2f plane. Therefore, instead of discrete frequency combs, we expect the generation of a spatial array of overlapping frequency-gradient comb spectra, each with a comb spacing of $\sim$ 50 MHz within the $\sim$ 50 GHz transmission envelope of the VIPA. Nevertheless, we will verify that this array will result in spatio-temporal steering in the far field as proposed in previous works [12], [13].

In Section 3.3 and Section 3.4, we present the beam steering results of the spatial array of resolved frequency combs described in Section 2.3.

3.2 Dynamically steered pulses from a mode-locked laser

To investigate the 2f plane, we conducted measurements by scanning an SMF connected to an OSA along the VIPA dispersion axis. The measurements were performed under the same experimental setup as the one described in Section 2.1 (Figure. 2.1). In that setup, different from the setup shown in Figure. 3.1, the 2f lens was a spherical lens with a focal length of 10 cm. It's worth noting that if a lens with a larger or smaller focal length was employed, it would result in a linear scaling of the dispersion axis on the 2f plane. Such scaling would lead to a smaller or larger dispersion rate, respectively. Therefore, in our measurement setup targeting the 4f plane (Figure. 3.1), the dispersion axis necessitates a scaling factor of 6/10 compared to the measurements conducted in this particular scenario, while the dispersion rate should be scaled up by a factor of 10/6.

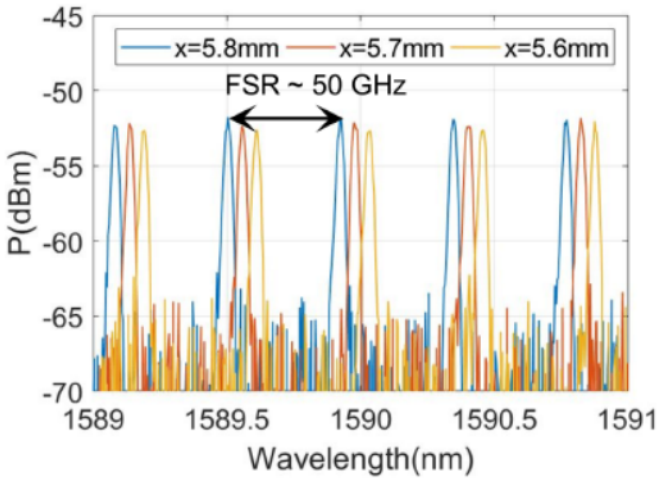

Figure 3.2. Spectra measured at three positions along x-axis in 2f plane at separations of 0.1 mm.

As expected, we observed a series of overlapping frequency-shifted spectra when scanning along the dispersion axis. Figure. 3.2 plots a section of the spectra measured at three different positions separated by 0.1 mm, each having a frequency spacing of $\sim$ 50 GHz between the spectral peaks, indicating the VIPA FSR, and a frequency shift of $\sim$ 6.5 GHz between each other. Due to the OSA's spectral resolution of 0.02 nm ($\sim$ 2.5 GHz), the individual comb lines of the mode-locked laser, spaced by $\sim$ 50 MHz, cannot be resolved. Figure. 3.3 illustrates the spectral peaks observed along the dispersion axis at increments of 0.1 mm. Consistent with the ASE and EO comb measurements, the frequency to space mapping is nearly linear, and 1mm along the dispersion axis yields a frequency shift of $\sim$ 0.5 nm. The FSR is calculated to be 50.0 ± 0.1 GHz.

Using the experimental setup described in Section 3.1 (Figure. 3.1), we measured the temporal profiles of the steered pulses on a 50 GHz bandwidth sampling scope. A portion of the input mode-locked laser is converted to an electric signal using a 12.5 GHz PD to trigger the sampling scope. While scanning along the x-axis, we observed temporal pulses that were delayed by $\sim$ 20 ps with respect to each other, as shown in Figure. 3.4. The temporal pulses exhibited a uniform spatial separation of 115 ± 5 μm. Given the demagnification factor of

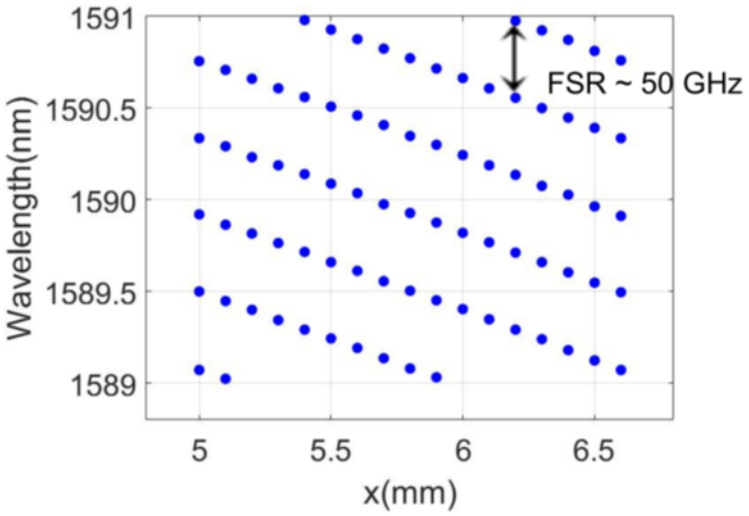

Figure 3.3. Spectral peaks measured along the dispersion axis on the 2f plane, with a step size of 0.1 mm.

~ 0.58 for the 4f system, this value closely matches the spacing of the reflections on the back plane of the VIPA, which is calculated to be 196 μm at the incident angle of 7.56°. The pulse waveforms were averaged 256 times on the scope and then curve-fitted using MATLAB. Figure. 3.5 illustrates the pulse-peak times, indicating a linear gradient in their delays. The fitted delay is 20.7 ± 1.4 ps, in agreement with the VIPA FSR. These results demonstrate the steering of ultrashort pulses ($\sim$ 100 ps duration) in discrete temporal steps of $\sim$ 20 ps in the far field.

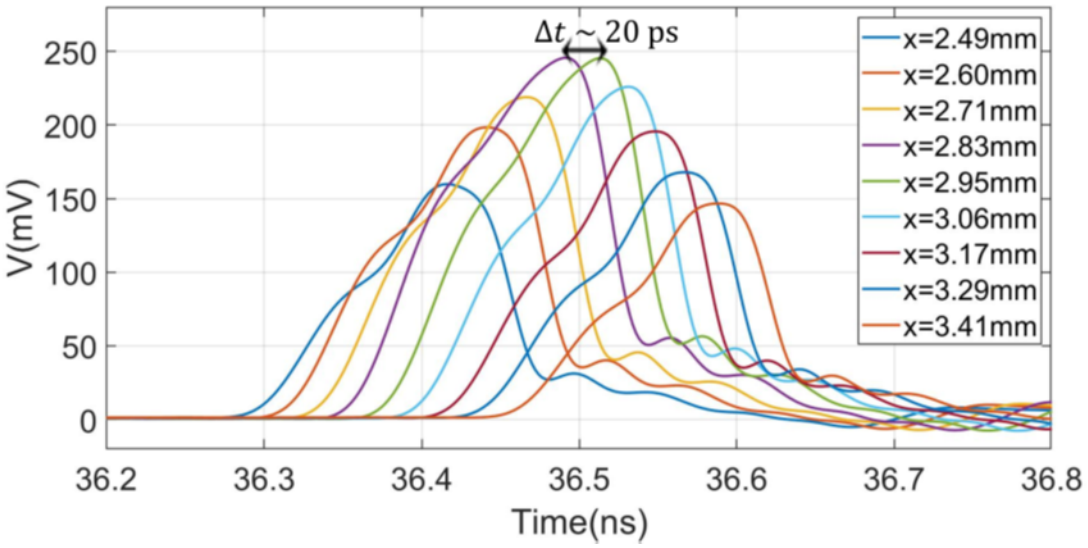

Figure 3.4. Temporal profiles of the delayed pulses measured on the 4f plane.

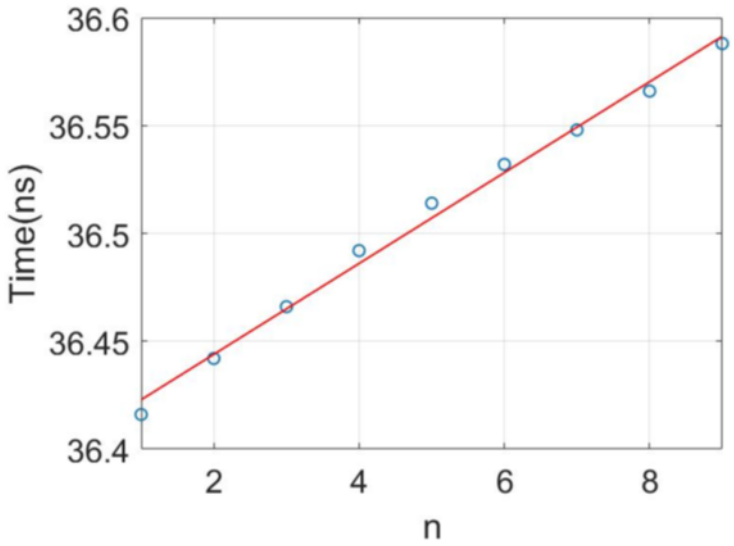

Figure 3.5. Pulse-peak times.

3.3 Spectral phase retrieval for steered pulses

As discussed in Section 2.2, the generated EO comb exhibits a nearly quadratic spectral phase across its spectrum. By compensating for this quadratic phase using a pulse shaper, transform-limited picosecond pulses can be obtained [25]. The sign of the quadratic phase is determined by the phase modulation provided by the PMs on the pseudo-square pulse train generated by the IM. Moreover, any deviation from the ideal 4f configuration in the setup may introduce additional quadratic spectral phase, similar to that of a grating-based pulse shaper [29]. This strong chirp, primarily caused by the EO comb generation process, leads to significant distortion of the steered pulses on the 4f plane (Figure. 3.10). To address this, we adopted a self-referenced and easy-to-implement technique [30] based on dual-quadrature spectral interferometry to retrieve the spectral phase of the steered pulses on the 4f plane. Subsequently, we compensated for the retrieved phase using a pulse shaper, effectively compressing the steered pulses.

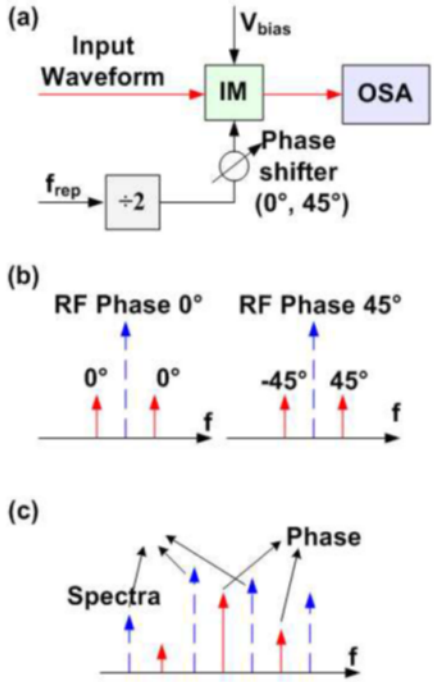

Figure 3.6. (a) Schematic of experimental setup. (b) The phase relation between the first-order sidebands at two moderating RF signal settings separated by 45 degrees. (c) Modulated spectra with interfering sidebands. [30]

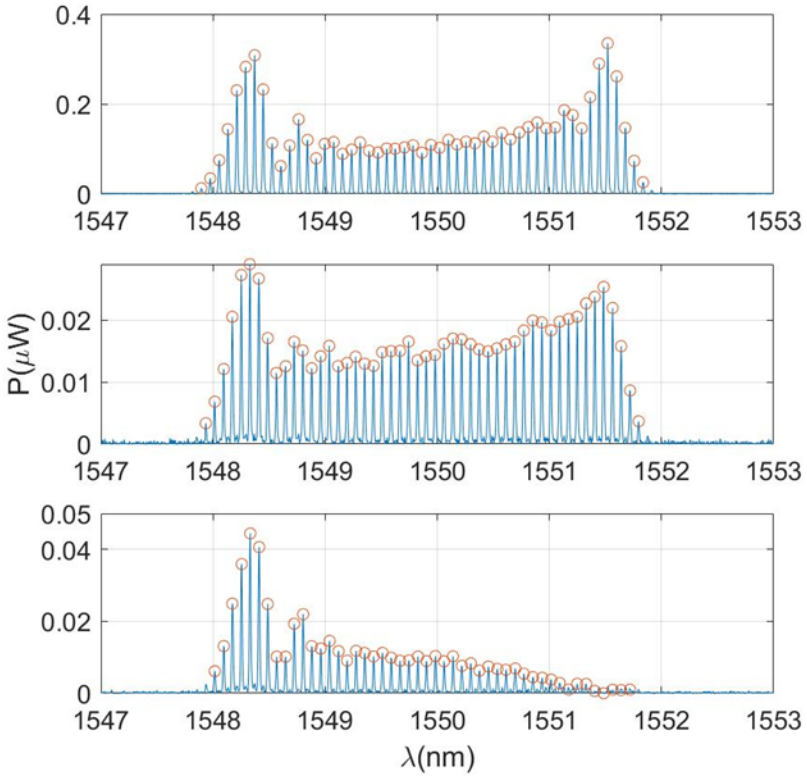

Figure 3.7. Original spectra (Top) and two modulated spectra (Bottom)

The experimental setup is illustrated in Figure. 3.6 (a). The generated EO comb was sent to an intensity modulator, which was driven by an RF signal at half the repetition frequency (f_{rep}) of the comb. The RF signal was divided from the same RF oscillator used for comb generation, and its phase was adjusted using a phase shifter. The power of the RF signal was set at a low level such that only first-order sidebands were generated and higher-order sidebands were negligible. Consequently, the first-order sidebands from adjacent comb lines would interfere with each other, resulting in a modulated comb line positioned in the middle of them (Figure. 3.6 (c)). The intensity of this modulated line relied on the spectral phase difference between the adjacent comb lines. As shown in Figure. 3.6 (b), when the phase of the RF signal is altered by 45 degrees, the phase difference of the first sidebands would change by 90 degrees. By measuring the spectra at the two different RF phase settings, namely the in-phase and quadrature cases, one could unambiguously retrieve the spectral phase from the interference lines observed in the two spectra. The original

spectrum, as well as the modulated spectra at the two RF phase settings, are shown in Figure. 3.7. During the measurement of the modulated spectra, the carrier comb lines were fully suppressed by adjusting the IM bias, with a carrier to first-order sideband ratio of 10 dB. This adjustment was made to minimize the contribution of the carrier lines to the measured sideband intensities due to the crosstalk of the OSA.

The intensities of the interfering sidebands are given by:

$$\begin{aligned} I_{inphase} &= C[|a_n|^2 + |a_{n+1}|^2 + 2|a_n||a_{n+1}| \cos(\phi_n - \phi_{n+1})] \\ I_{quadrature} &= C[|a_n|^2 + |a_{n+1}|^2 + 2|a_n||a_{n+1}| \sin(\phi_n - \phi_{n+1})] \end{aligned} \tag{3.1}$$

Where $|a_i|$ and ϕ_i are the spectral amplitude and phase of the original ith comb line, respectively, and C is the ratio between the sideband and carrier powers for a single frequency. By solving these two equations using spectral data, we were able to determine both C and the spectral phase differences for all the sidebands. Subsequently, the spectral phase of the original spectrum is obtained by summing up the spectral phase differences and is shown in Figure. 3.8. As expected, there is a dominant quadratic phase term present. The quadratic fit for the spectral phase is plotted in Figure. 3.9, with a quadratic coefficient of 3.17×10^{-4} radians/GHz^2.

To compress the steered pulses, we used a commercial pulse shaper to compensate for the retrieved quadratic phase. The linear term of the retrieved phase was neglected since it corresponds to a constant delay in the time domain. Similarly, the constant phase was also disregarded. The steered pulses on the 4f plane were detected using a 23 GHz photodetector and measured on a 50 GHz sampling scope. The measured pulse waveform before and after compression is shown in Figure. 3.10. After compression, the peak intensity doubled, and the measured pulse duration narrowed to $\sim$ 30 ps. The measured pulse duration is limited by the bandwidth of the detector, and the actual pulse duration can be accurately determined using autocorrelation techniques. For the case of a transform-limited pulse where the spectral phase is perfectly compensated, the calculated pulse duration is approximately 2 ps, corresponding to the $\sim$ 500 GHz bandwidth of the comb.

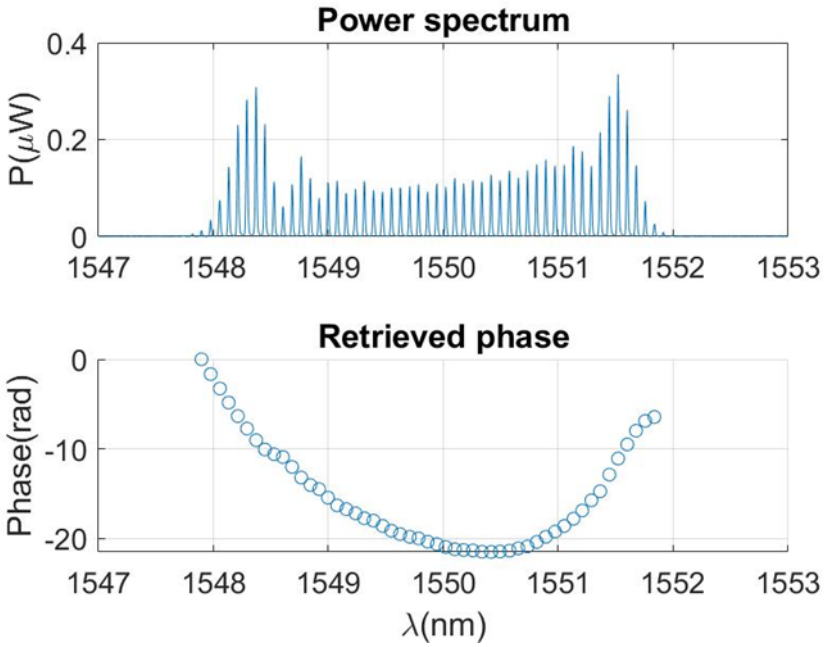

Figure 3.8. Retrieved spectral phase of the steered pulses

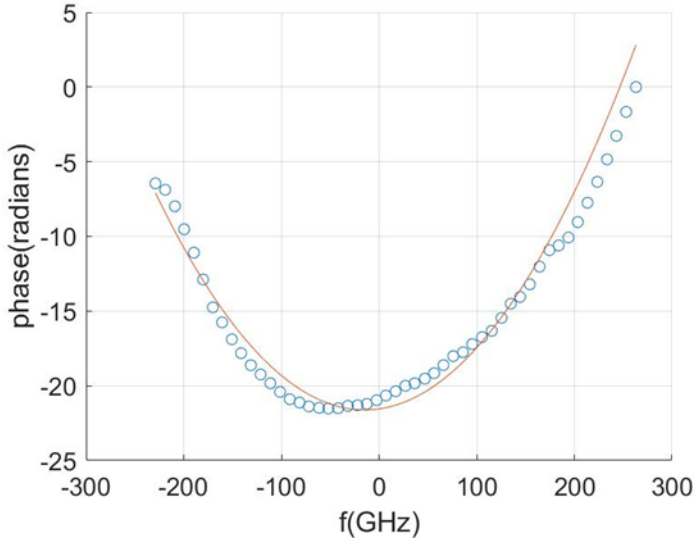

Figure 3.9. Quadratic fit for the retrieved spectral phase

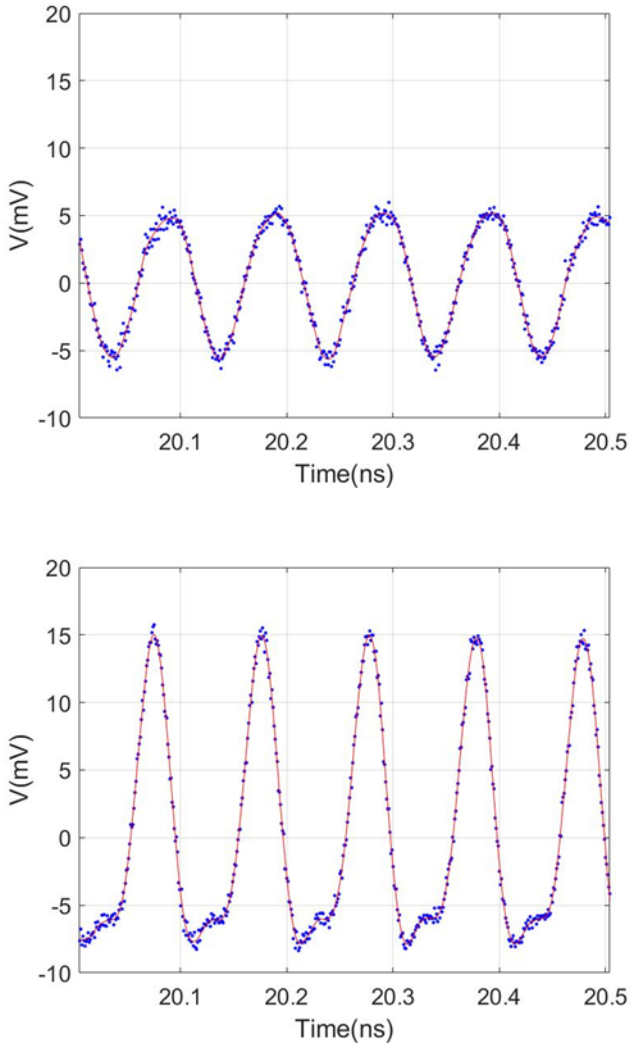

Figure 3.10. Temporal profile of the steered pulses: before (Top) and after (Bottom) pulse compression.

3.4 Dynamically steered pulses from an EO comb

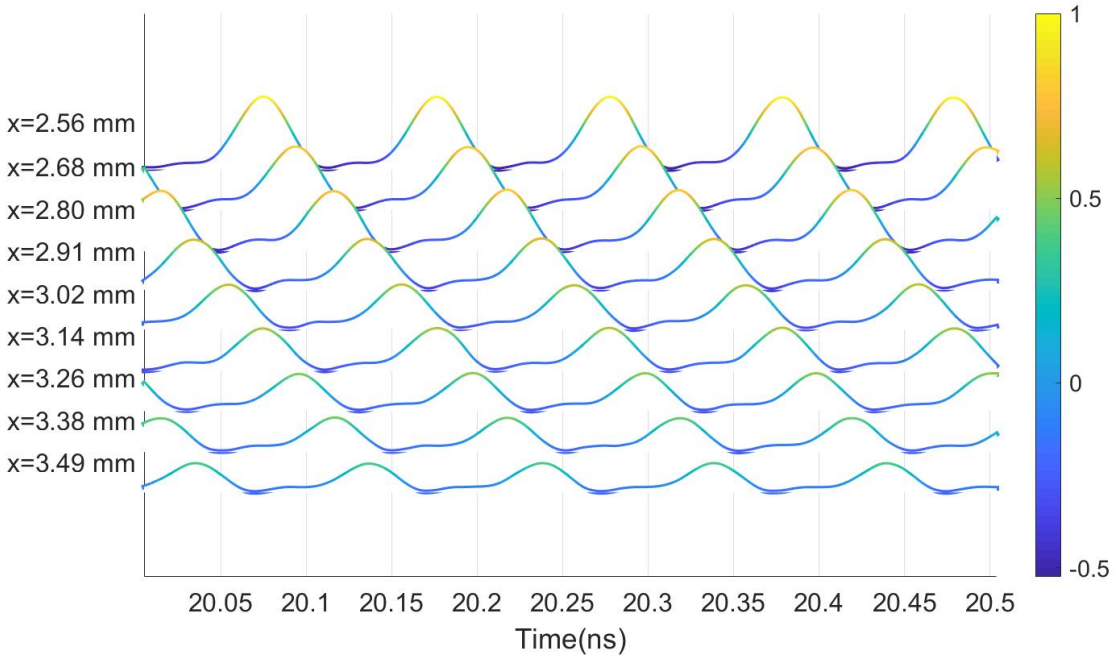

Figure 3.11. Temporal waveforms of the steered pulse trains on 4f plane

After compensating for the quadratic phase for the first steered pulse train, we proceeded to measure the temporal waveforms of the remaining steered pulse trains that were uniformly spaced on the 4f plane. These measurements were conducted under the same conditions as before, with the pulses being detected using a 23 GHz PD and measured on a 50 GHz sampling scope. A 10 MHz reference RF signal provided by the same RF oscillator used for EO comb generation was used as the trigger for the sampling scope. The pulse waveforms were averaged 256 times on the scope and then curve-fitted using MATLAB. All of the pulse trains were well compressed with a measured duration of $\sim$ 30 ps. This indicated that a similar amount of chirp was present in all of the steered pulses. Similar to the case of the mode-locked laser as input, the steered pulse trains exhibit a uniform spatial distribution with a spacing of $\sim$ 115 μm, agreeing with the demagnification factor of the 4f system. As shown in Figure. 3.11, each pulse train had a time period of $\sim$ 100 ps and was delayed by $\sim$ 20 ps with respect to each other. Figure. 3.12 illustrates the pulse-peak times of all pulse trains, indicating a linear gradient in their delays. The fitted delay, which corresponds to

the temporal pulsing rate, was 20.4 ± 0.2 ps, consistent with the FSR of the spatial array of frequency combs on the 2f plane. The time period, indicating the beam scanning rate, was averaged to be 101 ± 0.2 ps, aligning with the frequency gradient of the frequency comb array.

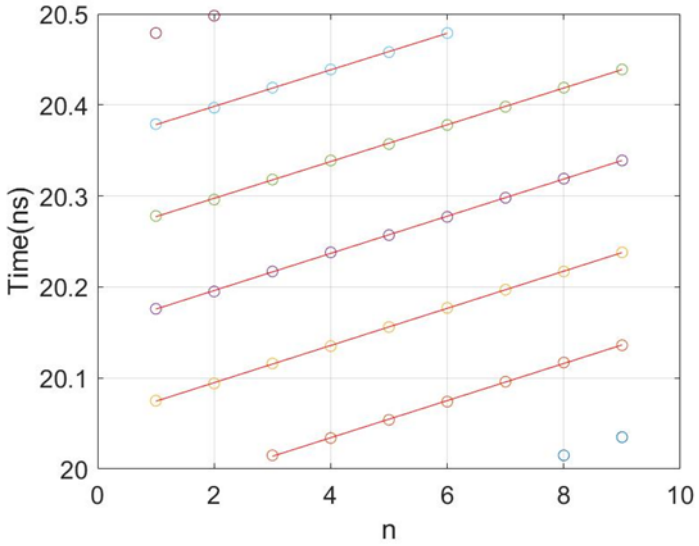

Figure 3.12. Pulse peak times of the nth steered pulse train

4. SUMMARY

This thesis presented an experimental demonstration of dynamic pulsed beam steering using a spatial array of frequency combs with a uniform gradient in their carrier-envelope offsets. To accomplish this, we leveraged the spectral dispersing capabilities of a VIPA to separate the different spectral lines of the input comb source, forming frequency-shifted spectra on the 2f plane of the VIPA. In Chapter 2, we successfully demonstrated a spatial array of resolved frequency combs derived from an EO comb input, exploiting the VIPA's high angular dispersion and small FSR. In Chapter 3, the dynamic spatio-temporal steering pattern observed on the 4f plane for both a mode-locked fiber laser and the EO comb was presented. Additionally, pulse compression for the EO comb was achieved through a self-referenced and easily implementable spectral phase retrieval technique. The experimental results successfully demonstrate the periodic scanning of ultrashort pulse trains in discrete spatial and temporal steps. Such scanning patterns could be significant for various LiDAR applications.

Moving forward, we are interested in (1) Measuring the duration of the steered pulses using autocorrelation techniques to verify the pulsed steering behavior. (2) Further investigating the beam steering far field by performing specific simulations based on VIPA properties and conducting measurements with higher resolution. (3) Exploring on-chip implementations of the demonstrated beam steering concept.

REFERENCES

[1] B. Behroozpour, P. A. Sandborn, M. C. Wu, and B. E. Boser, "Lidar system architectures and circuits," *IEEE Communications Magazine*, vol. 55, no. 10, pp. 135–142, 2017.

[2] C. V. Poulton, M. J. Byrd, P. Russo, *et al.*, "Long-range lidar and free-space data communication with high-performance optical phased arrays," *IEEE Journal of Selected Topics in Quantum Electronics*, vol. 25, no. 5, pp. 1–8, 2019.

[3] J. An, K. Won, Y. Kim, *et al.*, "Slim-panel holographic video display," *Nature communications*, vol. 11, no. 1, p. 5568, 2020.

[4] S. Lin, Y. Chen, and Z. J. Wong, "High-performance optical beam steering with nanophotonics," *Nanophotonics*, vol. 11, no. 11, pp. 2617–2638, 2022.

[5] I. Kim, R. J. Martins, J. Jang, *et al.*, "Nanophotonics for light detection and ranging technology," *Nature nanotechnology*, vol. 16, no. 5, pp. 508–524, 2021.

[6] C.-P. Hsu, B. Li, B. Solano-Rivas, *et al.*, "A review and perspective on optical phased array for automotive lidar," *IEEE Journal of Selected Topics in Quantum Electronics*, vol. 27, no. 1, pp. 1–16, 2020.

[7] P. Berini, "Optical beam steering using tunable metasurfaces," *ACS Photonics*, vol. 9, no. 7, pp. 2204–2218, 2022.

[8] M. J. Heck, "Highly integrated optical phased arrays: Photonic integrated circuits for optical beam shaping and beam steering," *Nanophotonics*, vol. 6, no. 1, pp. 93–107, 2017.

[9] J. A. Kong, *Electromagnetic wave theory*. EMW Publishing, 2008.

[10] K. Van Acoleyen, W. Bogaerts, J. Jágerská, N. Le Thomas, R. Houdré, and R. Baets, "Off-chip beam steering with a one-dimensional optical phased array on silicon-on-insulator," *Optics letters*, vol. 34, no. 9, pp. 1477–1479, 2009.

[11] G. Kang, S.-H. Kim, J.-B. You, *et al.*, "Silicon-based optical phased array using electro-optic *p*-i-*n* phase shifters," *IEEE Photonics Technology Letters*, vol. 31, no. 21, pp. 1685–1688, 2019.

[12] A. M. Shaltout, K. G. Lagoudakis, J. van de Groep, *et al.*, "Spatiotemporal light control with frequency-gradient metasurfaces," *Science*, vol. 365, no. 6451, pp. 374–377, 2019.

[13] S. Seshadri and A. M. Weiner, "All-optical dynamic pulsed beam steering," in *2022 Conference on Lasers and Electro-Optics (CLEO)*, IEEE, 2022, pp. 1–2.

[14] M. Shirasaki, "Large angular dispersion by a virtually imaged phased array and its application to a wavelength demultiplexer," *Optics letters*, vol. 21, no. 5, pp. 366–368, 1996.

[15] S. Xiao and A. M. Weiner, "An eight-channel hyperfine wavelength demultiplexer using a virtually imaged phased-array (vipa)," *IEEE photonics technology letters*, vol. 17, no. 2, pp. 372–374, 2005.

[16] S. Xiao and A. M. Weiner, "2-d wavelength demultiplexer with potential for 1000 channels in the c-band," *Optics Express*, vol. 12, no. 13, pp. 2895–2902, 2004.

[17] V. Supradeepa, C.-B. Huang, D. E. Leaird, and A. M. Weiner, "Femtosecond pulse shaping in two dimensions: Towards higher complexity optical waveforms.," *Optics express*, vol. 16, no. 16, pp. 11 878–11 887, 2008.

[18] S. A. Diddams, L. Hollberg, and V. Mbele, "Molecular fingerprinting with the resolved modes of a femtosecond laser frequency comb," *Nature*, vol. 445, no. 7128, pp. 627–630, 2007.

[19] G. Scarcelli and S. H. Yun, "Confocal brillouin microscopy for three-dimensional mechanical imaging," *Nature photonics*, vol. 2, no. 1, pp. 39–43, 2008.

[20] Z. Li, Z. Zang, Y. Han, L. Wu, and H. Fu, "Solid-state fmcw lidar with two-dimensional spectral scanning using a virtually imaged phased array," *Optics Express*, vol. 29, no. 11, pp. 16 547–16 562, 2021.

[21] M. Shirasaki, "Virtually imaged phased array," *Fujitsu Scientific & Technical Journal*, vol. 35, no. 1, pp. 113–125, 1999.

[22] S. Xiao, A. M. Weiner, and C. Lin, "A dispersion law for virtually imaged phased-array spectral dispersers based on paraxial wave theory," *IEEE journal of quantum electronics*, vol. 40, no. 4, pp. 420–426, 2004.

[23] S. Xiao, A. M. Weiner, and C. Lin, "Experimental and theoretical study of hyperfine wdm demultiplexer performance using the virtually imaged phased-array (vipa)," *Journal of lightwave technology*, vol. 23, no. 3, p. 1456, 2005.

[24] M. Shirasaki, A. Akhter, and C. Lin, "Virtually imaged phased array with graded reflectivity," *IEEE Photonics Technology Letters*, vol. 11, no. 11, pp. 1443–1445, 1999.

[25] A. J. Metcalf, V. Torres-Company, D. E. Leaird, and A. M. Weiner, "High-power broadly tunable electrooptic frequency comb generator," *IEEE Journal of Selected Topics in Quantum Electronics*, vol. 19, no. 6, pp. 231–236, 2013.

[26] V. Torres-Company and A. M. Weiner, "Optical frequency comb technology for ultra-broadband radio-frequency photonics," *Laser & Photonics Reviews*, vol. 8, no. 3, pp. 368–393, 2014.

[27] B. H. Kolner, "Space-time duality and the theory of temporal imaging," *IEEE Journal of Quantum Electronics*, vol. 30, no. 8, pp. 1951–1963, 1994.

[28] J. Azaña, "Time-to-frequency conversion using a single time lens," *Optics communications*, vol. 217, no. 1-6, pp. 205–209, 2003.

[29] A. M. Weiner, *Ultrafast optics*. John Wiley & Sons, 2011.

[30] V. Supradeepa, C. M. Long, D. E. Leaird, and A. M. Weiner, "Self-referenced characterization of optical frequency combs and arbitrary waveforms using a simple, linear, zero-delay implementation of spectral shearing interferometry," *Optics Express*, vol. 18, no. 17, pp. 18 171–18 179, 2010.